NSWC/DL TR-3449

DYNAMIC FRACTURE AND FRAGMENTATION OF CYLINDERS

by
C. ROBERT CROWE
WILLIAM H. HOLT
WILLIS MOCK, Jr.
O. HAYDEN GRIFFIN
Armaments Development Department

NOVEMBER 1976

NAVAL SURFACE WEAPONS CENTER
Dahlgren Laboratory
Dahlgren, Virginia 22448

NSWC

NAVAL SURFACE WEAPONS CENTER
DAHLGREN LABORATORY
Dahlgren, Virginia
22448

D. M. Agnew, Jr., Capt., USN
OIC and Assistant Commander

J. H. Mills, Jr.
Associate Technical Director

UNCLASSIFIED

SECURITY CLASSIFICATION OF THIS PAGE *(When Data Entered)*

REPORT DOCUMENTATION PAGE

READ INSTRUCTIONS BEFORE COMPLETING FORM

1. REPORT NUMBER: TR-3449	2. GOVT ACCESSION NO.
3. RECIPIENT'S CATALOG NUMBER	
4. TITLE *(and Subtitle)*: DYNAMIC FRACTURE AND FRAGMENTATION OF CYLINDERS,	5. TYPE OF REPORT & PERIOD COVERED: Final rept.
6. ~~PERFORMING ORG. REPORT~~ NUMBER	
7. AUTHOR(s): C. Robert Crowe, William H. Holt, Willis Mock, Jr., O. Hayden Griffin	8. CONTRACT OR GRANT NUMBER(s)
9. PERFORMING ORGANIZATION NAME AND ADDRESS: Naval Surface Weapons Center, Dahlgren Laboratory, Dahlgren, Virginia 22448	10. PROGRAM ELEMENT, PROJECT, TASK AREA & WORK UNIT NUMBERS
11. CONTROLLING OFFICE NAME AND ADDRESS	12. REPORT DATE: November 1976
	13. NUMBER OF PAGES: 65
14. MONITORING AGENCY NAME & ADDRESS*(if different from Controlling Office)*: NSWC/DL-TR-3449	15. SECURITY CLASS. *(of this report)*: UNCLASSIFIED
	15a. DECLASSIFICATION/DOWNGRADING SCHEDULE

16. DISTRIBUTION STATEMENT *(of this Report)*

Approved for public release; distribution unlimited.

F32353 F32353P

17. DISTRIBUTION STATEMENT *(of the abstract entered in Block 20, if different from Report)*

18. SUPPLEMENTARY NOTES

19. KEY WORDS *(Continue on reverse side if necessary and identify by block number)*

Fracture
Fragmentation
Shock Waves
Shear Banding
Solid Mechanics

20. ABSTRACT *(Continue on reverse side if necessary and identify by block number)*

An experimental and theoretical investigation of the mechanisms of fragmentation has been conducted for explosive-filled cylinders of Armco iron and HF-1 steel. Dynamic fracture nucleation and growth parameters for HF-1 steel were determined from gas gun experiments for use in computer modeling of the fracture and fragmentation processes. Calculated fragment mass distributions are compared with experimental results.

DD FORM 1 JAN 73 1473 EDITION OF 1 NOV 65 IS OBSOLETE

S/N 0102-LF-014-6601

UNCLASSIFIED

SECURITY CLASSIFICATION OF THIS PAGE *(When Data Entered)*

3125

FOREWORD

A joint NSWC/DL and Stanford Research Institute (SRI) experimental and computational effort has been carried out to develop a quantitative description of the fracture and fragmentation of explosive-filled cylinders. The approach is based on previously developed SRI models for fracture processes. This report presents the NSWC/DL part of the work and briefly describes the SRI part. The work was supported by NAVSEA Task No. SF 32-353-302 and by NSWC/DL Independent Research Funds.

This report has been reviewed and approved by C. A. Cooper, Head, Munitions Division.

Released by:

CDR G. J. FLANNERY
Assistant Head
Military Applications
Armaments Development Department

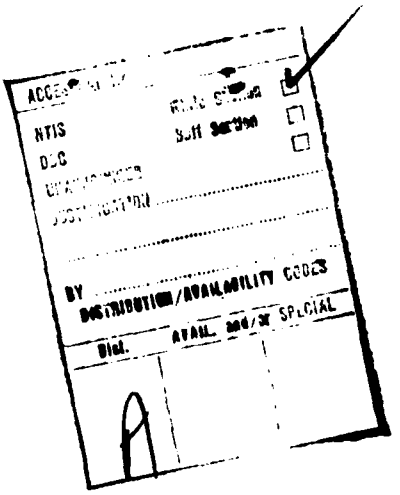

ACKNOWLEDGEMENTS

The authors would like to acknowledge the assistance of B. P. Durrer for crack counting, R. R. Retter for scanning electron microscopy assistance, D. D. Eller for metallography, M. R. Jamison and E. T. Shelton for cylinder fragmentation experiments, J. B. Bickley for assistance with the gas gun experiments, W. E. McLaughlin and J. L. East for computer programming, and J. R. Coughlin for HEMP code calculations.

The authors would also like to acknowledge L. Seaman, D. A. Shockey, and D. R. Curran of the Stanford Research Institute for helpful discussions.

TABLE OF CONTENTS

LIST OF ILLUSTRATIONS

LIST OF ILLUSTRATIONS (Continued)

LIST OF TABLES

EXECUTIVE SUMMARY

A joint NSWC/DL and Stanford Research Institute (SRI) experimental and analytical effort has been carried out to predict the fragmentation performance of explosive-filled metal cylinders. The approach is based on computational models that have been developed by SRI to describe the radial fracture and shear deformation processes that occur in cylinder fragmentation. The approach utilizes very high strain rate material parameters that are determined from gas gun impact experiments on small specimens. These parameters are used in computational models for the nucleation and growth of cracks in the material. Thermo-mechanical data are used in modeling of the shear deformation. The procedure has been applied to explosive-filled cylinders of Armco iron and HF-1 steel. Computational results for the fragment mass distributions show favorable agreement with experimental distributions.

I. INTRODUCTION

The design of a fragmentation warhead is influenced by many factors, including cost, logistics, safety, and effectiveness in damaging a target. The design objective is to maximize target damage, consistent with the other factors. A basic problem is to design the warhead to have fragments with the mass distribution, velocities, and angular distributions needed to defeat the target in an anticipated type of encounter. Experience derived from years of extensive testing of prototype warheads has shown that the fragment directions are controlled mainly by warhead geometry; however, the fragment mass distribution depends on the metal case thickness, explosive-mass to metal-mass ratio, and the metallurgical properties of the case material. While these general facts are known, adequate theoretical models for predicting the fragmentation behavior of a given warhead configuration have not evolved. A predictive capability for fragmentation would permit the computational optimization of warhead design for given target and launch conditions, and would minimize the costly, time-consuming testing of prototypes.

A new quantitative approach to the description of fracture and fragmentation processes has led to a predictive capability for armor penetration problems;[1] the work described herein is part of a joint effort by NSWC/DL and the Stanford Research Institute (SRI) to apply this approach to predict the fragment mass distribution (Mott plot) for an explosive-filled metal cylinder. The new approach involves experimental determination of the very high strain rate ($\gtrsim 10^5 s^{-1}$) fracture response of a material and computational modeling of the fracture and fragmentation processes. Fracture data for a material are obtained from gas gun impact and soft recovery experiments on small specimens. These data are used to obtain crack nucleation and growth (NAG) parameters that quantify the processes leading to fragmentation.[2]

When the explosive in a cylindrical warhead is detonated, the initial stresses in the cylinder wall are caused by explosive shock waves; these

stresses cause rapid outward acceleration of the wall. After the initial shock waves have subsided, the stresses in the cylinder wall are mainly those caused by the outward displacement. As cracks are formed and grow, the fracture surfaces eventually intersect to form surfaces of individual fragments. Previous investigations indicate that there are two types of macroscopic fracture contributing to the fragmentation of cylinders: localized shearing and radial cracking (Figure 1).

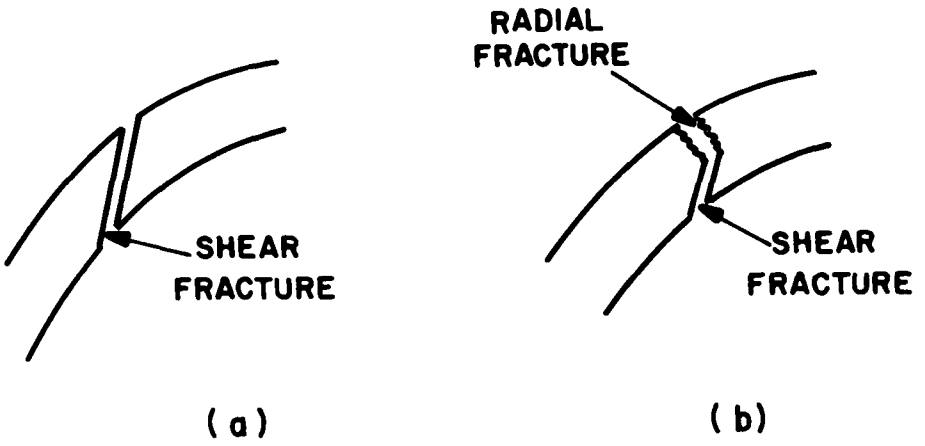

Figure 1. Two types of fracture occuring in cylinder fragmentation: (a) pure shear fracture and (b) bimodal fracture.

As part of the joint experimental and analytical effort, a computational model for predicting the fragmentation of a cylinder was developed by SRI. The brittle fracture and fragmentation (NAG/FRAG) model[3] previously developed by SRI was modified to apply to the radial cracking. A shear nucleation and growth (SNAG) model was developed for the shear fractures. Details of the SNAG model development are given in Reference 4. The NSWC/DL work in support of this effort included gas gun experiments to determine fracture nucleation and growth parameters for HF-1 steel and explosive fragmentation experiments to obtain fragment mass distributions for cylinders of Armco iron and HF-1 steel.

A brief historical background of cylinder fragmentation is presented in Chapter II. Chapter III contains the conventional mechanical properties for Armco iron and HF-1 steel. Determination of the HF-1 steel NAG parameters is discussed in Chapter IV. The fragmentation experiments are described in Chapter V. Shear band models and a comparison of the experimental and SRI-calculated fragment mass distributions are given in Chapter VI. Chapter VII contains a summary and recommendations for future work.

II. HISTORICAL BACKGROUND

During World War II, considerable research was directed towards solving the fragmentation problem. Most notable are the works of Taylor[5, 6] and Mott.[7-9] Taylor devised models to describe the fragmentation of cylindrical bombs and analyzed the stress state associated with the cylinder radius at which fractures penetrated the wall. He presented data showing that detonation gases did not escape through the wall until a cylinder had expanded to nearly double its initial diameter. He showed that the initial explosive-induced circumferential stresses near the inner surface of the cylinder are compressive. Thus, radial fractures that are started at the outer surface by tensile stresses could be expected to extend into the material only to a depth at which the stresses become compressive. Shear fractures could occur in the compressive region, but these fractures would not open to allow gases to escape until the circumferential compression becomes zero. The predictions of this theory are in general agreement with experimental observations, although there are some discrepencies with regard to details.

Mott also calculated the stress distribution in a rapidly expanding cylinder and used a Griffith[10] crack model in an attempt to predict the propagation of cracks in the cylinder wall. He also developed a theory for the distribution of radial fractures in tubular bombs that were constructed of stacked rings around a thin cylindrical shell and filled with explosive. The theory incorporates the effects of local

stress reduction due to relief waves that propagate from the fracture surfaces as soon as a crack forms. The cracks were assumed to start at inherent material flaws that had a Gaussian size distribution. While this theory is generally assumed to be inadequate, Mott and Linfoot[7] found experimentally that the fragment mass distribution for most projectiles and cylindrical warheads can be approximated by an empirical equation of the form

$$N(>m) = N_o \exp [- (m/\mu)^{1/2}] \quad (1)$$

where $N(>m)$ is the number of fragments with mass greater than m, N_o is the total number of fragments from the warhead, m is the fragment mass group, and μ is a fragmentation size parameter. The exponent 1/2 in Equation (1) applies for fragmentation processes where the wall thickness controls one of the fragment dimensions. When the wall is thicker than the average fragment thickness, the exponent 1/3 is used. Figure 2 is a plot of Equation (1). The representation of fragmentation data in this form has been in use since Mott's original work.

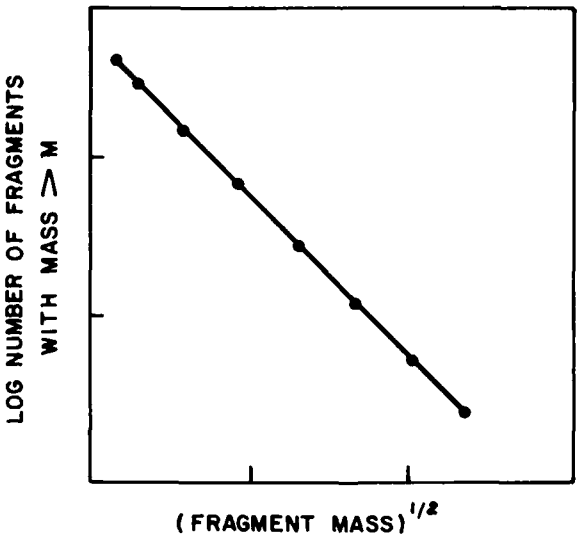

Figure 2. Graphical representation of the fragment mass distribution from an exploded cylinder (Mott plot).

There have been many other attempts to relate the dynamic processes in fragmentation to the warhead geometry, warhead case material properties, and the properties of the explosive.

Rinehart and Pearson[11] have proposed a model of fragmentation in which fracturing occurs when the radial particle velocity in the cylinder material exceeds a critical straining velocity. The model predicts the number of fragments to be proportional to the ratio of the radial particle velocity and the critical straining velocity.

A more thorough treatment of the fragmenting bomb problem has been carried out by Hoggatt and Recht[12] using basically the same approach as used by Taylor. They assumed that the high pressure from the explosive causes small radial cracks to appear in the tensile circumferential stress region near the outer surface of the cylinder. Within this stress region, cylinder expansion occurs by extrusion which actuates shear planes in the inner compressive circumferential stress region. This model treats the stress distribution in detail and includes the effects of unstable thermoplastic shear. The unstable shear occurs when the material in the shear zone is thermally softened by the heat generated in plastic deformation; the local flow stresses decrease with increasing strain.

Banks[13] has observed that the number of cracks in a cylinder increases linearly with the radial velocity of the cylinder wall at the time of break-up, as was predicted by Mott. In this work, no consideration was given to the absolute number of cracks and the velocities considered were not representative of those normally observed in fragmentation weapons.

High-speed photography of fragmenting cylinder by Rinehart and Pearson,[14] Kronman,[15] and Clark[16] has shown that cracks start at an expansion ratio of approximately 1.2 and detonation gases appear from the cracks at an expansion ratio of approximately 1.8. These observations are consistent with the predictions of Taylor and those of Hoggatt and Recht. In a series of experiments by Clark and Juriaco,[17] it was shown

that the number of cracks in an expanding cylinder can be correlated with Mott's predictions to an accuracy of ±20 percent through the use of room temperature static mechanical properties and one adjustable parameter.

Meinert[18] has attempted to relate fragmentation behavior to the static fracture energy, defined as the area under a conventional stress-strain curve. Bardes[19] reports that a linear relationship exists between the μ of Equation (1) and the percent reduction in area for a conventional tensile test for HF-1 steel. Work by Magis[20, 21] and others[22-24] has been directed toward correlating fragment size distributions with composition, heat treatment, and mechanical properties. Magis considered eight parameters: charge-mass to metal-mass ratio (c/m), outside diameter, tensile strength, yield strength, percent reduction of area, percent elongation, Charpy impact strength, and hardness for 10 different steels including three heat treatments of HF-1 steel. He found that only three parameters (c/m, outside diameter, and percent elongation) were statistically correlated for all the steels. The other parameters had statistical correlation only in individual steels.

Bardes investigated the effects of specific microconstituents on fragmentation behavior. This work showed that adiabatic shearing is essentially independent of microstructure, carbide networks at grain boundaries affect fragment size, large-grained structures produce small fragments, homogenation produces large fragments, and decarburization has no effect. The effect of the carbide network has also been noted by Clark and Juriaco; and, work by O'Shea[25] confirms the effect of grain size on fragmentation behavior.

More recently, effort has centered around predicting fragmentation behavior through the use of computer codes. The HEMP and FRAG 2 codes have been used in fragmentation studies at NSWC/DL.[26] In HEMP calculations fragmentation is introduced artifically through an additional operation: an experimentally determined average fragment mass for a Mott distribution

is applied to the HEMP results. This approach yields a distribution that agrees with experimental results when fragments from all polar zones are considered together, provided the correct average mass has been selected for the computation. This procedure does not match the distribution for individual polar zones. FRAG 2 utilizes the Magis data to calculate the distribution per polar zone by calculating a distribution for elemental rings spaced along the length of the projectile, and by utilizing a scaling equation to correct for changes in ring size. The results obtained with FRAG 2 are inadequate because of the limitations of the Magis data and the inability to predict the experimental mass distribution per polar zone.

III. MATERIALS

The Armco iron used for this work was obtained from the Corey Steel Company as a 12.7-cm-diameter hot-rolled bar. The HF-1 steel was obtained from Norris Industries as 12.7-cm-diameter cylinders and hot-rolled bar. The manufacturer's chemical analysis of the Armco iron and the NSWC/DL chemical analysis of the HF-1 steel are given in Table 1.

Table 1. Chemical analysis of materials.

Element (Wt %)	Armco Iron	HF-1 Steel
C	0.004	1.08
P	Tr	0.011
S	0.025	0.0001
Al	0.0002	0.006
Si	Tr	0.86
Mn	Tr	1.83
Mo	Tr	0.07
Ni	0.0001	Tr
Cr	Tr	0.15
O	0.010	--
N	0.001	--
Cd	0.003	--
Mg	0.001	--

The Armco iron was used in the as-received condition. The structure, as shown in Figure 3(a), is basically a single-phase polycrystalline aggregate with ASTM grain size number of approximately 2.5 to 3. A few inclusions are also present; these probably are oxides. The final structure for the HF-1 steel after heat treatment is shown in Figure 3(b). It consists primarily of tempered martensite with some dispersed carbide precipitates and retained austenite. Stress-strain curves for Armco iron and HF-1 steel are shown in Figures 4 and 5, respectively. Relevant mechanical data for these materials are listed in Table 2.

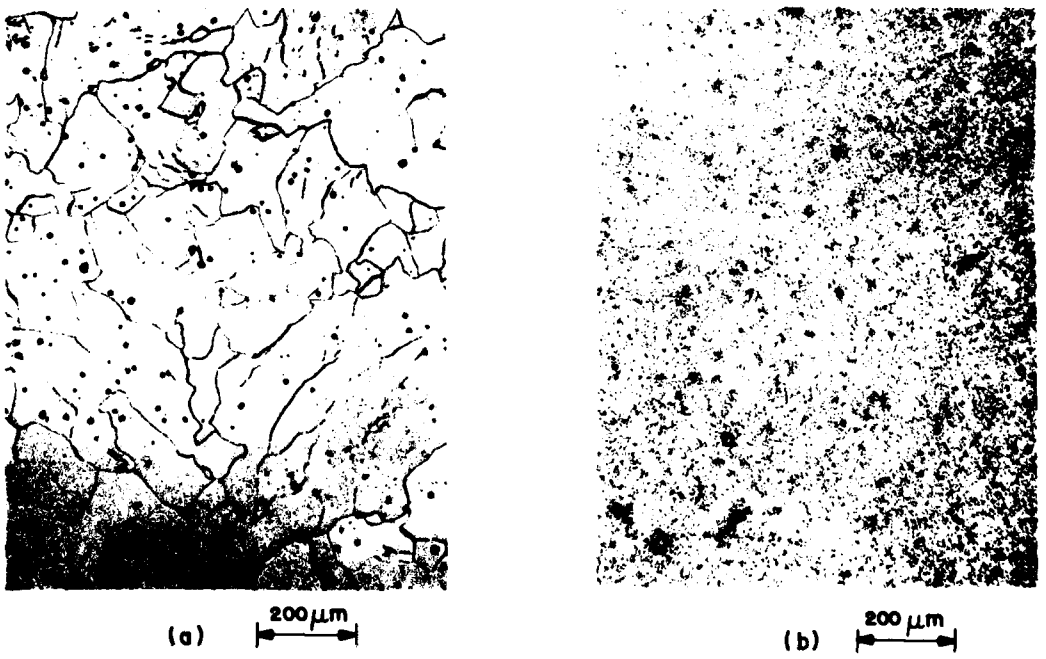

Figure 3. Microstructure of materials: (a) Armco iron and (b) HF-1 steel.

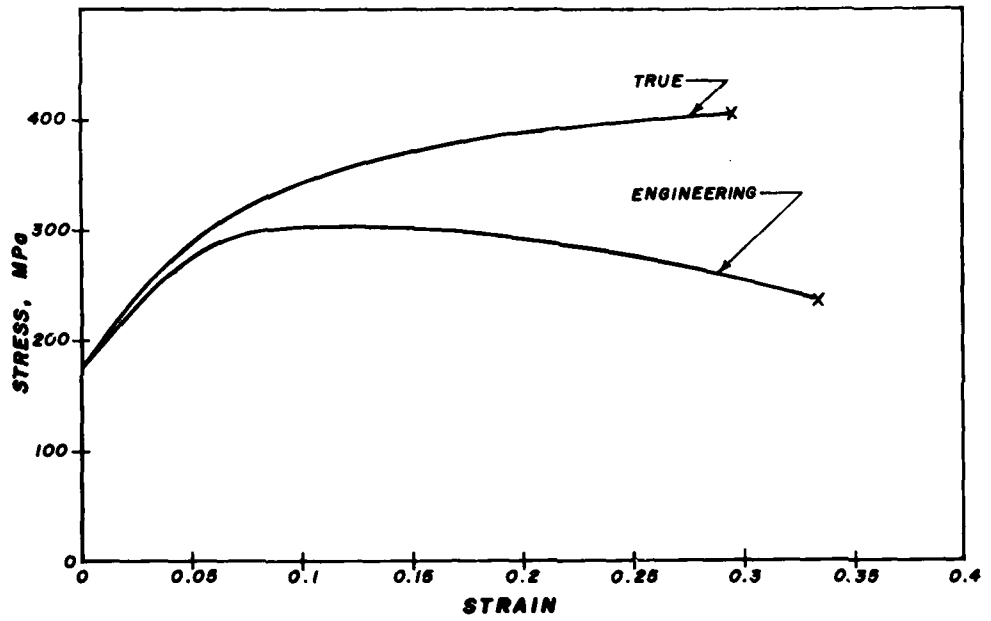

Figure 4. True stress-strain and engineering stress-strain curves for Armco iron.

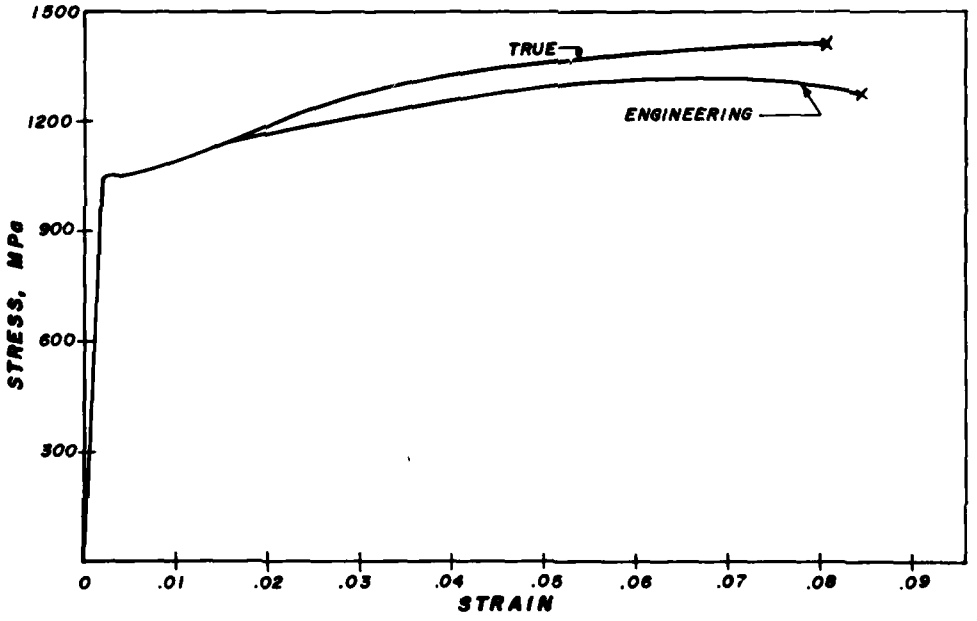

Figure 5. True stress-strain and engineering stress-strain curves for HF-1 steel.

Table 2. Mechanical properties of materials.

	0.2-Percent Yield Stress (MPa*)	Ultimate Tensile Strength (MPa)	Hardness
Armco Iron	180	300	R_b 40
HF-1 Steel	1040	1320	R_c 40

* 1 megapascal (MPa) = 145.0 psi, 1 gigapascal (GPa) = 10^3 MPa

IV. DETERMINATION OF FRACTURE NUCLEATION AND GROWTH PARAMETERS FOR HF-1 STEEL

A. INTRODUCTION

This chapter describes the method for obtaining the NAG parameters for HF-1 steel. The method developed by SRI for other materials[3, 27] has been followed, with minor exceptions. The parameters are used in the SRI brittle fracture model to predict radial crack formation in cylinder fragmentation (Figure 1). The steps to obtain the NAG parameters are described briefly as follows: Instrumented gas gun experiments are performed to determine the shock wave equation of state of the material. A series of soft recovery gas gun experiments is performed to produce differing amounts of internal fracture in the specimens under known shock-loading conditions. The recovered specimens are sectioned on a diameter and polished to reveal the microscopic spall fracture. The number of cracks, their sizes, and orientations with respect to the impact plane are digitized. These surface distributions are converted to volume distributions using the SRI BABS2 computer code. The stress state in the material is determined with the SRI PUFF code. PUFF is a finite-difference wave propagation code that calculates the stress state in stepwise time increments. A PUFF computation is made using the NAG model and a first-estimate set of parameters. This computation yields a volume distribution of cracks which is compared with an experimental

distribution; the values of the NAG parameters in PUFF are adjusted until agreement is obtained.

B. DYNAMIC FRACTURE EXPERIMENTS

Instrumented gas gun experiments[28] were performed to measure the dynamic yield stress (also called the Hugoniot elastic limit) and the elastic wave velocity in HF-1 steel. A Hugoniot elastic limit of 2.3 GPa and an elastic wave velocity of 5.94 km/s were measured.[29]

When performing the spall fracture experiments, the impacted specimen is soft recovered to minimize any unintentional damage.[30] This is accomplished by the post-impact separation and in-flight capture of the projectile and impactor; the specimen is soft recovered in a container filled with rags. A target assembly for a spall fracture experiment is shown in Figure 6. The gun bore diameter is 40 mm. The projectile velocity is measured at impact with the three velocity pins. The barrel is evacuated to minimize gas cushion effects on impact. The specimen is held in a stainless steel mounting ring by a low-melting-point alloy.

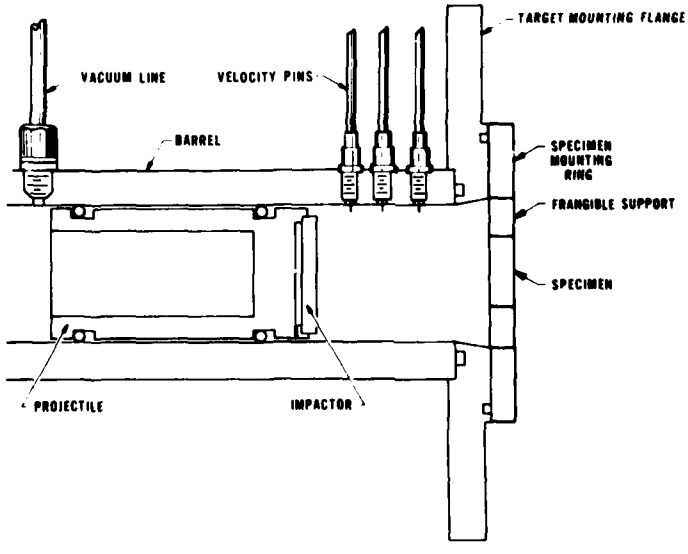

Figure 6. Schematic of muzzle region with specimen assembly for spall fracture experiment.

For spall fracture to occur, the experimental conditions must cause tensile stresses in the specimen. Figure 7 is a simplified schematic of the spall process. The impactor thickness is less than the specimen thickness. In the first step after impact, a plane shock wave propagates into both impactor and specimen. In the next step, one wave reaches the back surface of the impactor while the other wave continues into the specimen. The wave in the impactor is reflected as a rarefaction wave and propagates back through the impactor, toward the specimen. Subsequently, a rarefaction wave moves into the specimen from its free surface. When the two plane rarefaction waves interact, the result is a tensile stress in the specimen. This tensile stress occurs because in rarefaction waves, material is accelerated in a direction opposite to the rarefaction propagation direction. If the tensile stress amplitude and duration are sufficient, incipient spall fracture occurs.

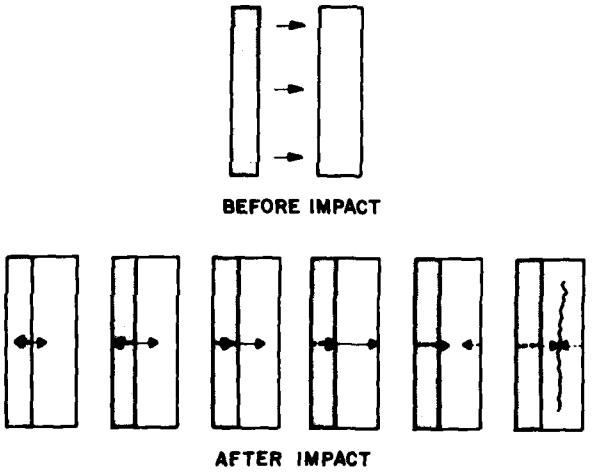

Figure 7. Simplified schematic of the spall process. After impact the time sequence of wave interactions is shown from left to right. The solid and dashed lines indicate the propagation of compression and rarefaction waves, respectively.

The fracture process is characterized by a threshold stress for crack or void nucleation as well as the other material-dependent NAG

parameters. Thus, controlled stress conditions will result in controlled amounts of spall-fracture damage. The stress amplitude is determined from the impact velocity and the previously measured shock properties of the materials used. The stress duration is controlled by the thickness of the impactor; the larger the thickness, the larger the duration of the stress.

A summary of the spall fracture experiments performed to obtain the NAG parameters for HF-1 steel is presented in Table 3. The last column of the table gives a qualitative degree of damage for the specimens as determined by microscopic observation. Typical tensile stress amplitudes ranged from about 2 to 5 GPa, and typical stress durations were fractions of a microsecond.

Table 3. Spall fracture experiments for HF-1 steel.

Number	Projectile Velocity (km/s)	Driver Thickness (mm)	Sample Thickness (mm)	Qualitative Degree of Damage
89	0.120	1.609	3.179	No Visible Damage
95	0.130	2.369	6.318	Incipent
111	0.193	1.156	3.185	Light
112	0.204	1.159	3.192	Light
110	0.149	2.371	6.348	Light
92	0.180	2.372	6.336	Light
113	0.202	1.596	3.189	Medium
98	0.160	2.372	6.349	Medium
91	0.183	2.373	6.337	Medium
90	0.191	2.370	6.361	Heavy
94	0.200	2.369	6.355	Heavy
88	0.276	1.596	3.190	Full Separation

C. PROCEDURE FOR OBTAINING CRACK DISTRIBUTIONS

To obtain crack distributions, the recovered and sectioned specimens (Figure 8) are first macrophotographed at 5X magnification using a Bausch and Lomb L camera. During this procedure, it is very important to illuminate the specimen with diffuse light so that all the

cracks are visible in the photograph. Figures 9 and 10 are composites of these photographs for selected specimens. For crack counting, each 5X photograph was enlarged again and arranged together to form a 25X composite of the specimen surface.

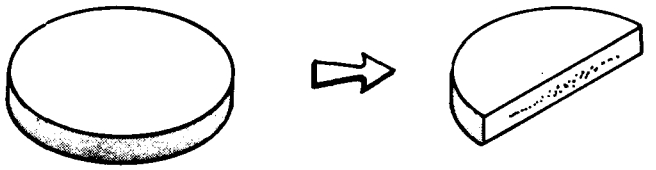

Figure 8. Sectioning of specimen to reveal fracture damage.

The 25X composite was mounted on a Computer Equipment Corporation Model TF-10C Digitizer to determine the coordinates of the cracks. The general data reduction criteria used was to count the longest segment as a crack and each intersecting segment as a crack. If the intersecting crack extended through the primary crack, its length was taken as extending from tip to tip. If the intersecting crack stopped at the primary crack or appeared to extend through the primary crack with a relative displacement, each segment was treated as an individual crack.

The digitized data were then used as input to a computer program that divides the damaged region into ten zones parallel to the specimen faces, calculates the length, orientation, and location of the midpoint of each crack relative to the impact surface, and assigns each crack to a zone based on the location of the midpoint. This program was written to interface with the SRI BABS2 program. The computer-generated representation of the digitized surface crack data for a specimen is shown in Figure 11. The volume distribution of cracks for a specimen is shown in Figure 12. This distribution is represented

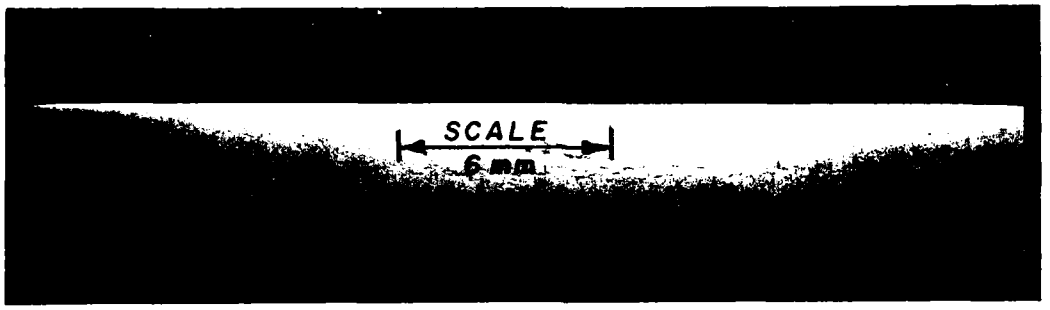

(a) SHOT 111, 0.193 km/s

(b) SHOT 112, 0.204 km/s

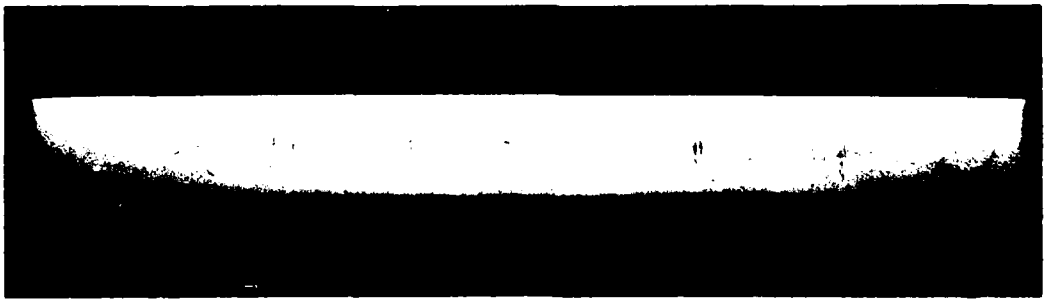

(c) SHOT 113, 0.202 km/s

Figure 9. Macrophotographs of 7.2-mm-thick specimens showing microscopic spall fracture.

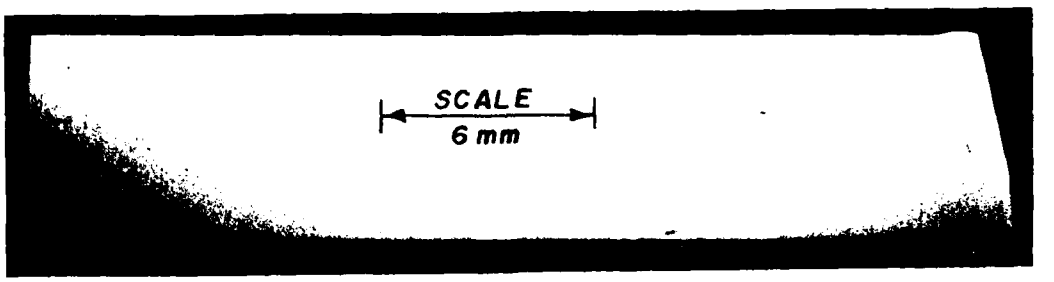

(a) SHOT 95, 0.130 km/s

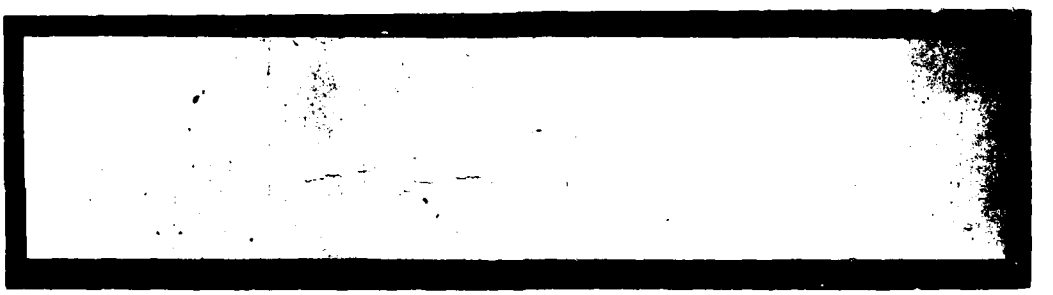

(b) SHOT 98, 0.160 km/s

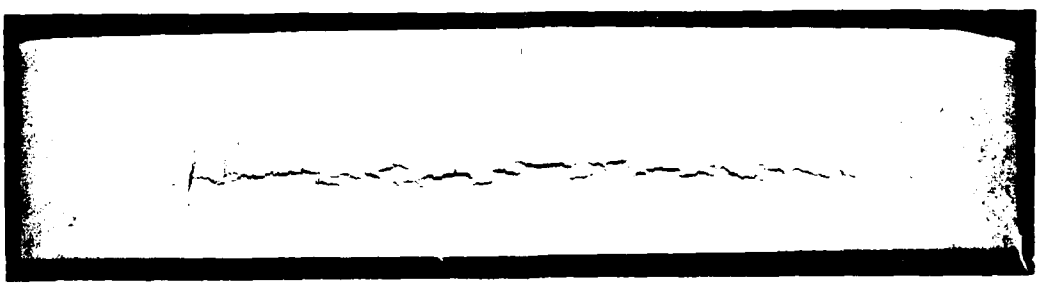

(c) SHOT 94, 0.200 km/s

Figure 10. Macrophotographs of 6.3-mm-thick specimens showing microscopic spall fracture.

by a plot showing the number of cracks having a radius R (crack half-length) greater than a certain value. To eliminate the effects due to relief waves from the edge of the specimens, only fracture data central to the damaged region were used.

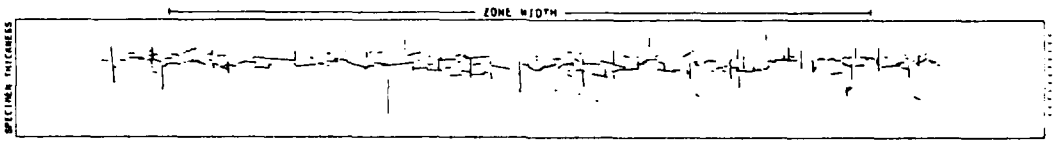

Figure 11. Computer plot of the surface distribution of cracks for a specimen. The marks on the specimen edge indicate the boundaries for the ten damage zones.

D. CALCULATION OF NAG PARAMETERS

The volume crack distributions are quantified by fitting a straight line to the data corresponding to zone of maximum damage for each specimen. This straight line fit (Figure 12) is represented by the equation

$$N_g = N_o \exp(-R/R_1) \qquad (2)$$

where N_g is the number of cracks per unit volume with radius greater than R, N_o is the total number of cracks generated per unit volume, and R_1 is related to the final size of the cracks. Values of N_o and R_1 are determined for each specimen.

The maximum tensile stress and tensile duration are then determined for each specimen using the PUFF code and allowing no fracture to occur. The quantities obtained from the computation are the peak tensile stress σ_m and the tensile duration Δt. The tensile duration is the time for which a threshold stress value is exceeded.

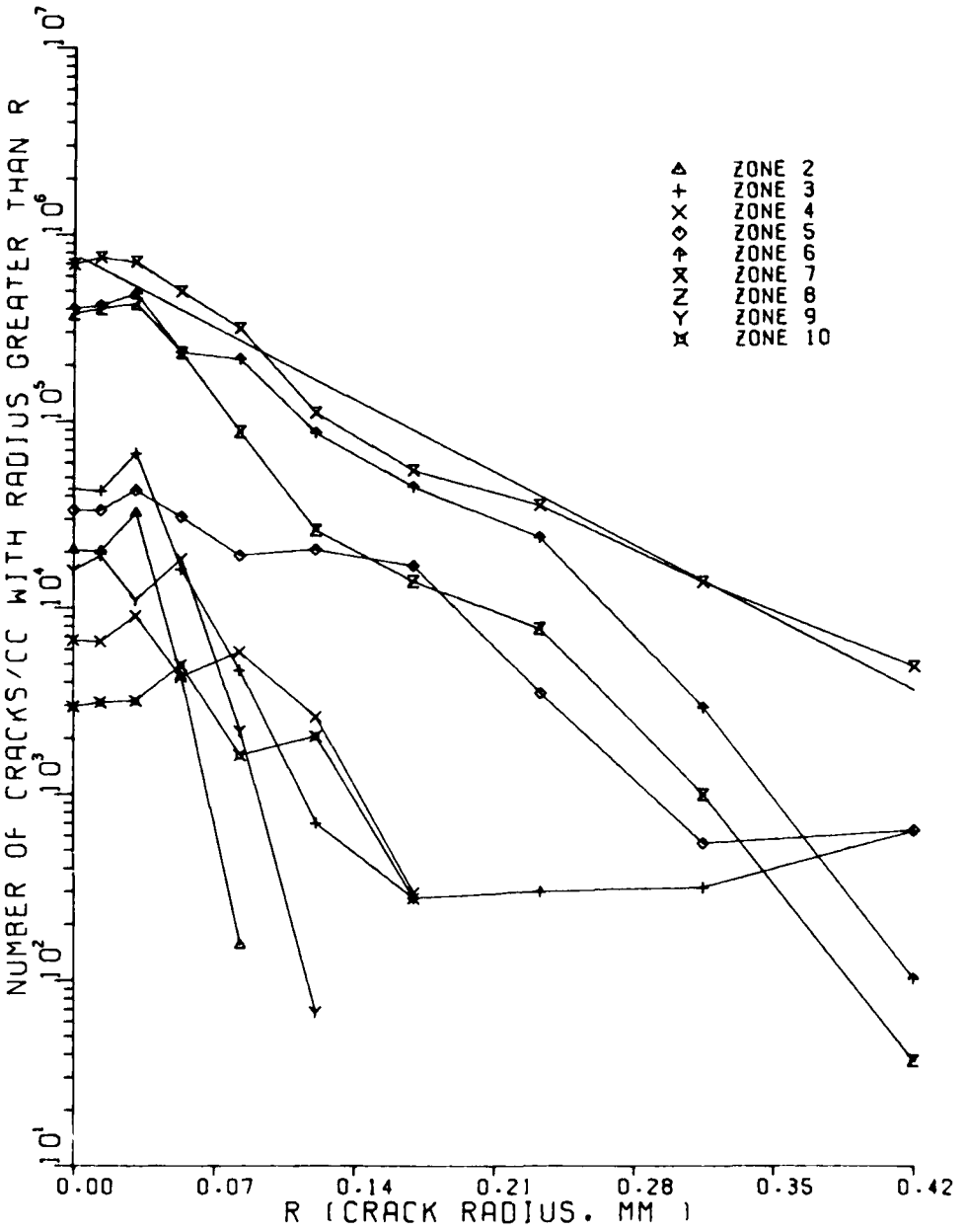

Figure 12. Computer plot of the volume distribution of cracks for a specimen.

The quantities N_o, R_1, Δt, and σ_m are used to form the first estimates of the NAG parameters. The nucleation rate for cracks $\dot{N}$ and the growth rate for cracks $\dot{R}$ are given by

$$\dot{N} = \dot{N}_o \exp\left[\frac{\sigma - \sigma_{no}}{\sigma_1}\right] \tag{3}$$

and

$$\dot{R} = T_1(\sigma-\sigma_{go})R \tag{4}$$

where σ is the applied stress and R is the crack radius. The NAG parameters are $\dot{N}_o$, σ_1, σ_{no}, σ_{go}, T_1, and R_o. R_o is the crack radius at nucleation and is defined in Equation (5).

A first estimate for the threshold nucleation rate $\dot{N}_o$ and the nucleation sensitivity σ_1 is obtained by plotting the values $\ln(N_o/\Delta t)$ versus σ_m for each of the specimens and fitting the points to Equation (3). σ_{no} is the threshold stress. The growth coefficient T_1 and the nucleation size parameter R_o are obtained by plotting the values $\ln R_1$ versus $\sigma_m \Delta t$ for each of the specimens and fitting the points to the equation

$$\ln R_1 = \ln R_o + T_1 \sigma_m \Delta t \tag{5}$$

which is obtained by integrating Equation (4), assuming the growth threshold parameter σ_{go} to be negligible. The material viscosity η is obtained from the equation $T_1 = 1/4\eta$. The dynamic plain-strain fracture toughness K_{IC} is obtained from the equation $\sigma_{go} = (\pi/4R)^{1/2} K_{IC}$.

These NAG parameter estimates are then used as input to a PUFF computation, which allows fracture to occur. New calculated values for N_o and R_1 are obtained from the PUFF output and compared with the experimental values. If agreement is not obtained, the parameters $\dot{N}_o$ and T_1

are adjusted and the computation is repeated. This iterative process is continued until the experimental and computed values agree. The NAG parameters determined for HF-1 steel are given in Table 4. Also included for comparison are the SRI-determined parameters for Armco iron.

Table 4. Dynamic fracture parameters for HF-1 steel and Armco iron.

Parameter	Units	HF-1 Steel	Armco Iron*
T_1	$cm^2/dyn\text{-}s$	5.25×10^{-5}	6.0×10^{-4}
σ_{go}	dyn/cm^2	1.0×10^{9}	2.0×10^{8}
R_o	cm	5.5×10^{-3}	5.0×10^{-5}
$\dot{N}_o$	$no./cm^3\text{-}s$	4.0×10^{10}	4.6×10^{12}
σ_{no}	dyn/cm^2	2.0×10^{10}	3.0×10^{9}
σ_1	dyn/cm^2	1.0×10^{9}	4.56×10^{9}

* Reference 1

V. EXPLODING CYLINDER EXPERIMENTS

A. INTRODUCTION

Two types of experiments were performed to provide information on the expansion and fragmentation of explosive-filled cylinders: (1) sawdust pit experiments to provide fragments exhibiting both radial and shear fractures for model development and to provide the fragment mass distributions, and (2) a framing camera experiment to provide cylinder strain data. The test configurations consisted of cast-in-place composition B explosive which extended beyond the cylinder to minimize end effects (Figure 13). Configuration details are given in Table 5.

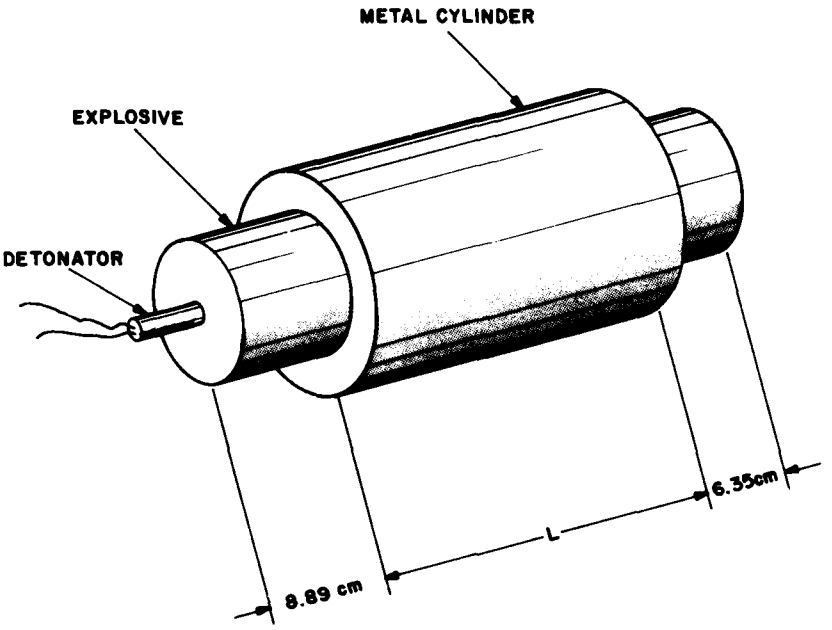

Figure 13. Schematic of exploding cylinder experiment.

Table 5. Configuration details for exploding cylinder experiments.

Experiment Number	Test Type	Material	I.D. (cm)	O.D. (cm)	L. (cm)	Explosive Charge (kg)
1	Pit	Armco Iron	7.62	11.43	20.3	2.77
2	Pit	Armco Iron	7.62	11.43	20.3	2.76
3	Pit	HF-1 Steel	7.62	12.07	20.3	2.75
4	Pit	HF-1 Steel	7.62	12.07	20.3	2.75
5	Framing Camera	Armco Iron	7.62	11.43	38.1	4.10

B. SAWDUST PIT EXPERIMENTS

These experiments were conducted at the NSWC/DL Sawdust Pit Facility.[31] Following detonation, the fragments were captured in a large volume of sawdust, and then were recovered by screen and magnetic separation techniques. Mass distributions were determined by weighing and counting each fragment with mass greater than 1 grain (64.8 mg). Fragments smaller than this were not counted, but the total weight was recorded. In all experiments, at least 99.5 percent metal mass was recovered.

Fragment mass distributions determined from the pit experiments are shown in Figures 14 and 15. Both the Armco iron and HF-1 steel distributions deviated from linear behavior at large fragment masses. This is not unusual because of the small statistical sample in the highest mass classes. The Armco iron cylinders also deviated from linear behavior in the low mass classes. This is considered to be an actual feature of the distribution and not due to secondary breakup of the fragments during recovery since Armco iron is a tough and ductile material compared with the HF-1 steel (which did not deviate from linear behavior).

C. METALLOGRAPHIC OBSERVATIONS OF RECOVERED FRAGMENTS

The microstructural features of representative fragments were investigated by metallographic procedures. Selected fragments of Armco iron and HF-1 steel are shown in Figure 16. The fragments had well-defined fracture surfaces which were preserved with Krylon lacquer. Laboratory specimens were prepared by sectioning the fragments to reveal a through-thickness plane normal to the cylinder axis. The specimens were mounted and polished, and then etched (2-percent Nital solution) to reveal the microstructural features of interest. Specimen examination was performed with a Bausch and Lomb Research II Metallograph.

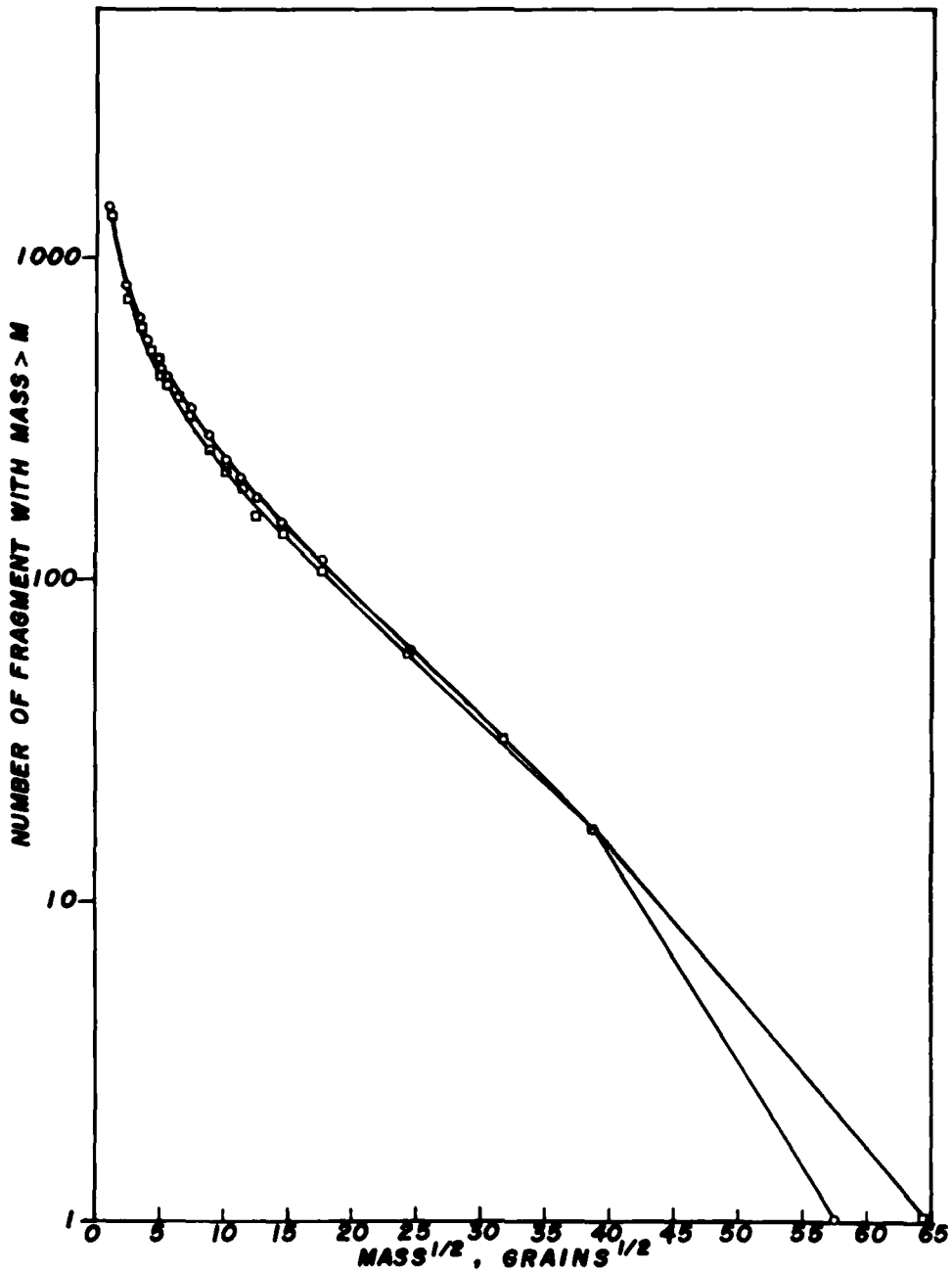

Figure 14. Fragment mass distributions for Armco iron cylinders.

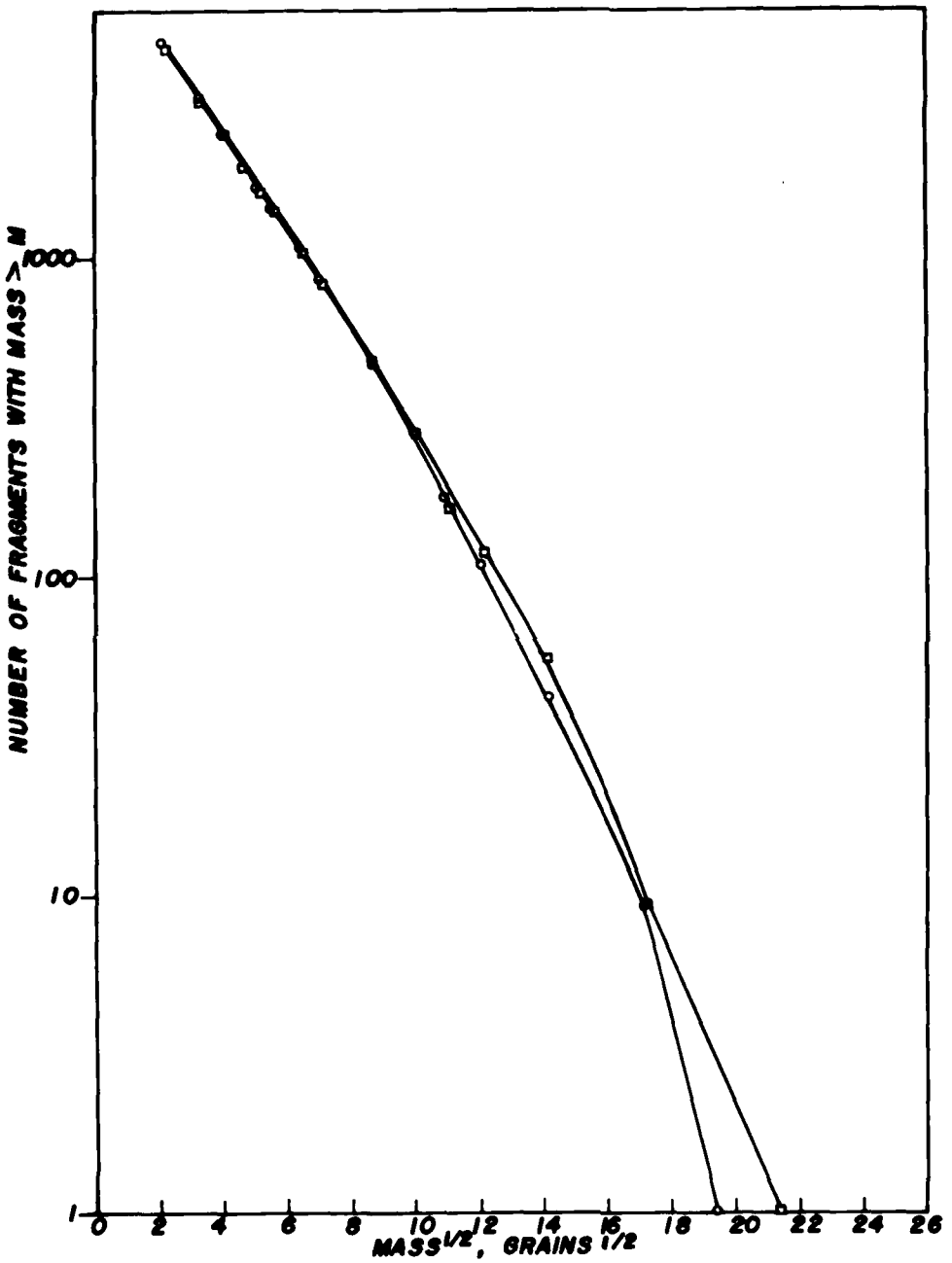

Figure 15. Fragment mass distributions for HF-1 steel cylinders.

Figure 16. Fragments of Armco iron (upper in figure) and HF-1 steel (lower in figure) used in metallographic and SEM studies.

Fracture surfaces were examined with a Cambridge MARK II-A scanning electron microscope (SEM). To prepare the SEM specimens, the clear lacquer was removed by soaking the fragments in acetone. The fracture surfaces were then cleaned ultrasonically in a solution consisting of 3-ml hydrochloric acid (sp. gr. 1.19), 4-ml 2-Butyne-1,4-diol (3.5 percent aqueous solution), and 50-ml deionized water.[32] This method also removed cellulose fibers from the sawdust which had become imbedded in the fracture surfaces during recovery. The fragments were cemented to aluminum disks with an electrically-conductive silver paste so that the fracture surfaces could be viewed in the SEM.

Figure 17 shows cross-section specimens of Armco iron and HF-1 steel. Both specimens exhibited bimodal fracture. For convenience of discussion, the specimens are divided into three regions in a radial direction. In Region 1 (approximately the outer one-half thickness) the

specimens exhibited transgranular cleavage on planes roughly normal to the tangential direction. While both metals showed internal cracking, the cracks in HF-1 steel were fewer in number and longer in length. These cracks remained sharp, with no evidence of crack-tip blunting due to plastic deformation [Figure 18(b)]. In Armco iron the cleavage cracks tended to be stacked in radial arrays with each individual crack approximately one grain diameter in length [Figure 18(a)]. The cracks exhibited blunting which progressed as the location of the cracks approached the transition Region 2. Those cracks near Region 2 were highly lenticular, suggesting a strong plastic deformation gradient.

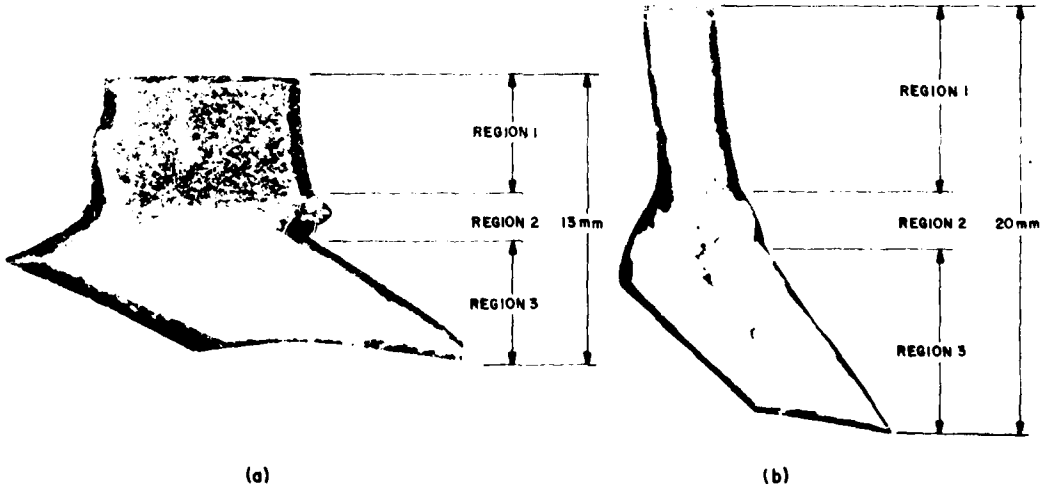

Figure 17. Cross-sections of recovered fragments: (a) Armco iron and (b) HF-1 steel.

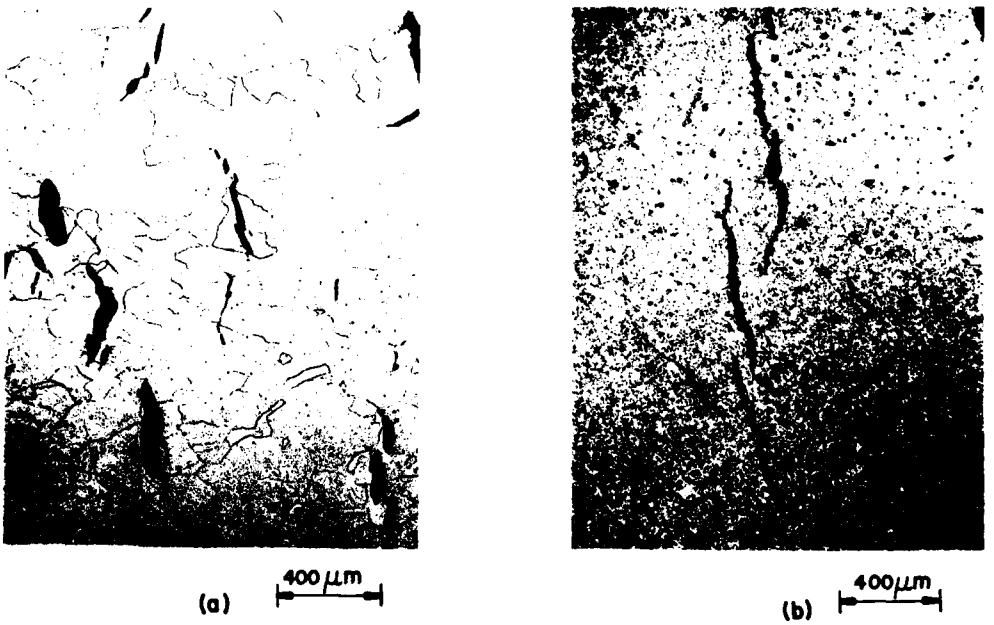

Figure 18. Internal cracks in Region 1: (a) Armco iron and and (b) HF-1 steel.

Figure 19(a) is an SEM micrograph of a radial fracture surface of Armco iron in Region 1. The fracture morophology consists of regions of quasi-cleavage and pure shear. This observation, in conjunction with Figure 18(a), suggests that in Armco iron the crack nucleation and the crack growth processes are different. Nucleation apparently occurs by cleavage of individual grains, whereas crack growth and link-up occur by void nucleation, growth, and coalescence. Figure 19(b) is an SEM micrograph of a radial fracture surface in HF-1 steel. The fracture morphology again consists of regions of quasi-cleavage and regions of void coalescence. This morphology compares favorably with that observed in spalled gas-gun specimens. The scale of the fracture is finer in the fragments than in the spall specimens, and the spall specimens exhibit more cleavage. The difference in the two cases may result from the larger hydrostatic compression that occurs during cylinder fracture.

Seaman et al.[4] have observed crack blunting in Armco iron fragments supplied to them for metallurgical examination. They suggest that this fracture morphology is produced by tensile cleavage of individual grains, the arrest of these cracks at grain boundaries, and the subsequent plastic stretching at the crack tips.

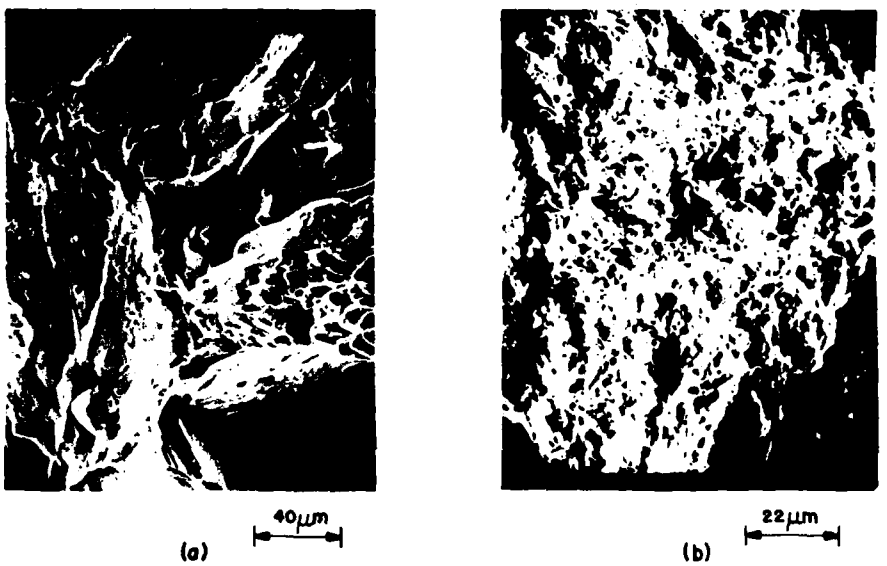

Figure 19. SEM micrographs of radial fractures in Region 1: (a) Armco iron and (b) HF-1 steel.

Another important feature of the microstructure in Region 1 is the distortion of the matrix material between radial fractures. Microhardness measurements across the thickness (Figure 20) indicate the relative degrees of material hardening. Armco iron shows a strong strain gradient in the middle third of the thickness, whereas HF-1 steel shows a more gradual trend. To estimate the tangential strain in this region, one can consider constant-volume spherical grains shearing to form ellipsoids of the same volume. If x and y are the major and minor ellipsoid axes, respectively, the tangential strain is approximately

$$\varepsilon_t \simeq \ln \left[1 + \frac{x - 3(xy^2)^{1/3}}{3(xy^2)^{1/3}} \right] . \qquad (6)$$

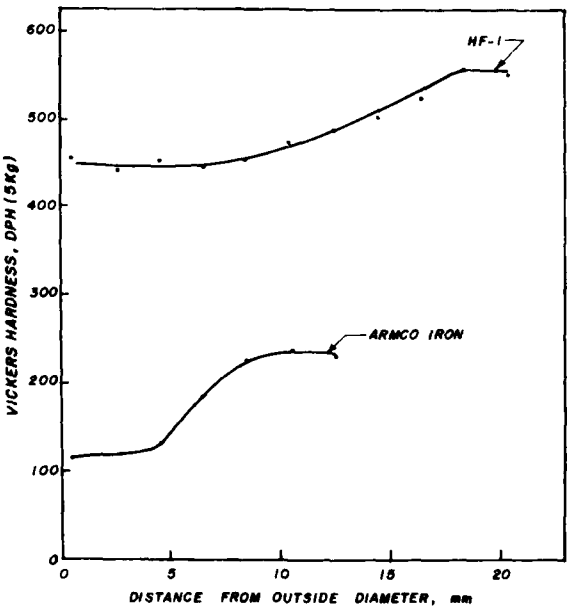

Figure 20. Microhardness profiles through the fragment thickness.

Since the virgin Armco iron (Figure 3) had an equiaxed-grain structure, Equation (6) can be used. An average over 15 grain diameters gives $\varepsilon_r \simeq 0.33$. Since stress relief associated with the formation of these fractures arrests matrix deformation, it is estimated that the radial fractures were formed approximately 13 μs after detonation. Bardes[19] obtained $\varepsilon_r = 1.8$ for an HF-1 steel cylinder with a carbide network and well-tempered martensite matrix.

In Region 3, the fracture surfaces were of the shear type in both materials. The Armco iron specimens (Figure 21) exhibited large grain distortions in the bulk, and unstable shear at the fracture surfaces and also at intervals within the bulk. Matrix deformation occurred by twinning and glide on closely spaced, wavy slip bands within each grain. Regions of highly localized shear were inclined approximately 45° to the cylinder radius, following the maximum shear trajectories in discrete packets. The deformation became less localized at the ends of these packets. At the intersection of each active shear trajectory with the

inner surface, a finite offset was observed. Seaman et al.[4], however, reported instances of active shear trajectories with no apparent offset at the inner surface.

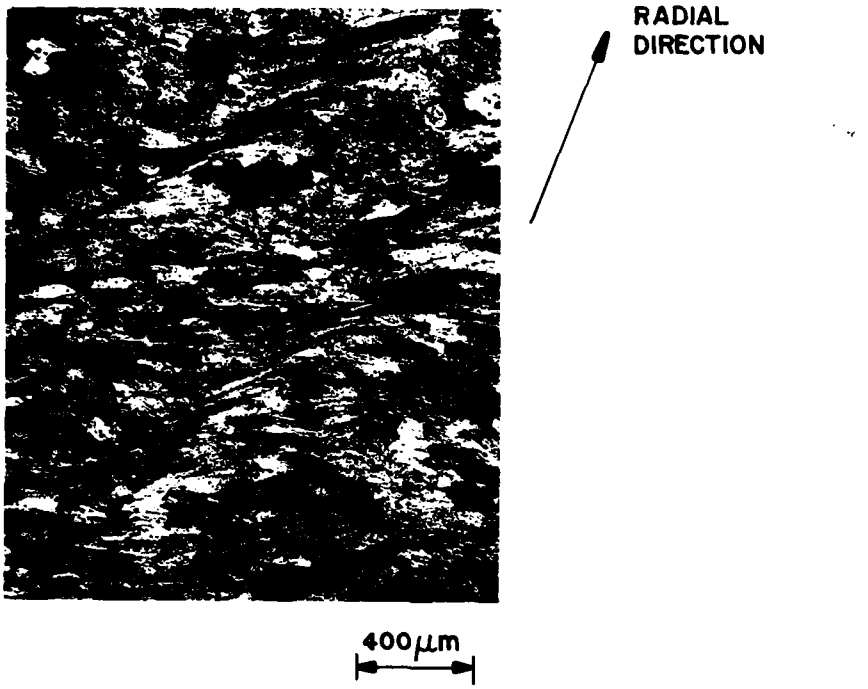

Figure 21. Micrograph showing localized shear deformation in Armco iron.

The spacing between the active shear trajectories in Armco iron that are bounded by fracture surfaces of the same rotation was approximately 1 to 5 mm. The shear packet width was approximately 200 μm, and the offset at the inner surface was typically 190 μm.

Observations on HF-1 fragments in Region 3 were somewhat different: bulk distortions were much less severe and localized shearing was of the transformation type. This phenomena, which has been widely observed in the high strain rate processing of steels, has been explained as localized shear heating to temperatures in the austenite phase field.[33] When the

deformation is complete (10 to 50 μs after detonation), there is a rapid quenching of the heated zone by the surrounding cooler material. This forms untempered martensite which is not attacked by the etching material because of the lack of ε-carbide precipitates in the substructure. Hence, a large portion of the shear zone is clearly delineated. Figure 22(a) shows a portion of a shear zone in HF-1 steel, and a crack associated with the untempered martensite.

Along a single shear trajectory which has a crack associated with it, there are often regions exhibiting crack openings in the bulk. This observation for HF-1 steel [Figure 22(b)] corresponds to the stop-start behavior in Armco iron and again suggests interior nucleation.

Shear zones of different rotation sometime intersect as shown in Figure 22(c). When this occurs, a convenient marker is provided for offset measurements. Here the offset associated with the primary shear is 250 μm, corresponding to an offset of 350 μm at the inner surface of the same primary shear. The spacing between active shear zones of the same rotation was between 320 and 1450 μm and the shear packet width in uncracked shear zones was 2.5 to 6.8 μm. The above metallographic observations are important for computational models of the shear phenomena and will be discussed further in the next chapter.

An SEM micrograph of the shear fracture in Armco iron is shown in Figure 23(a), where the fracture has occurred by void growth and coalescence. Figure 23(b) shows a higher magnification of one of the spheres in Figure 23(a). Quantitative dispersive X-ray analysis of the spheres failed to reveal any difference in composition between this feature and the matrix material. It is concluded that these features resulted from the collapse of very hot asperrities following separation. An SEM micrograph of the shear fracture in HF-1 steel is shown in Figure 24. The fracture again resulted from void coalescence. In this case, however, the scale is much finer than in Armco iron.

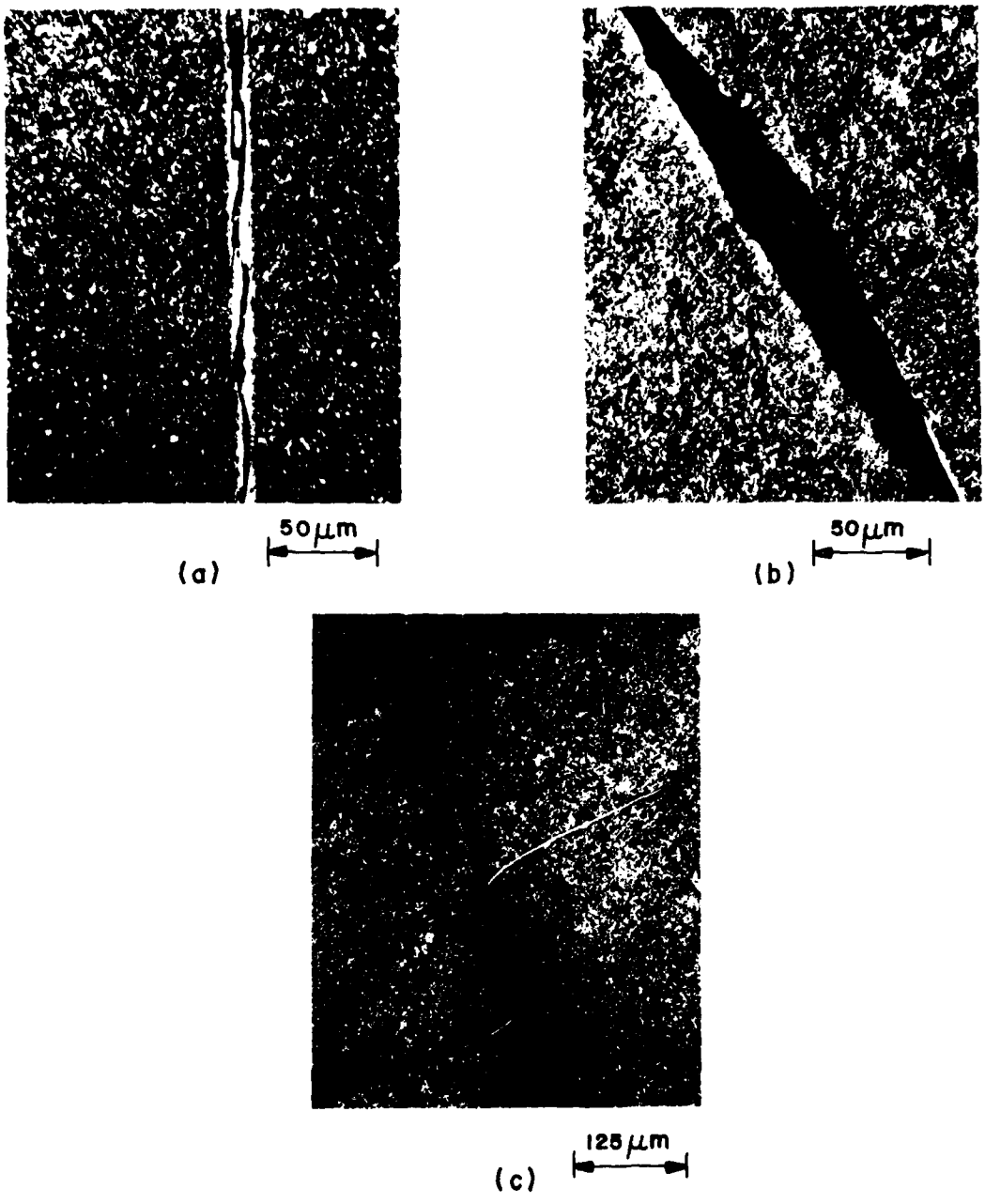

Figure 22. Micrograph of HF-1 steel fragments showing: (a) portions of a localized shear band, (b) crack opening within the bulk material at a shear band, and (c) intersecting shear bands of different rotation.

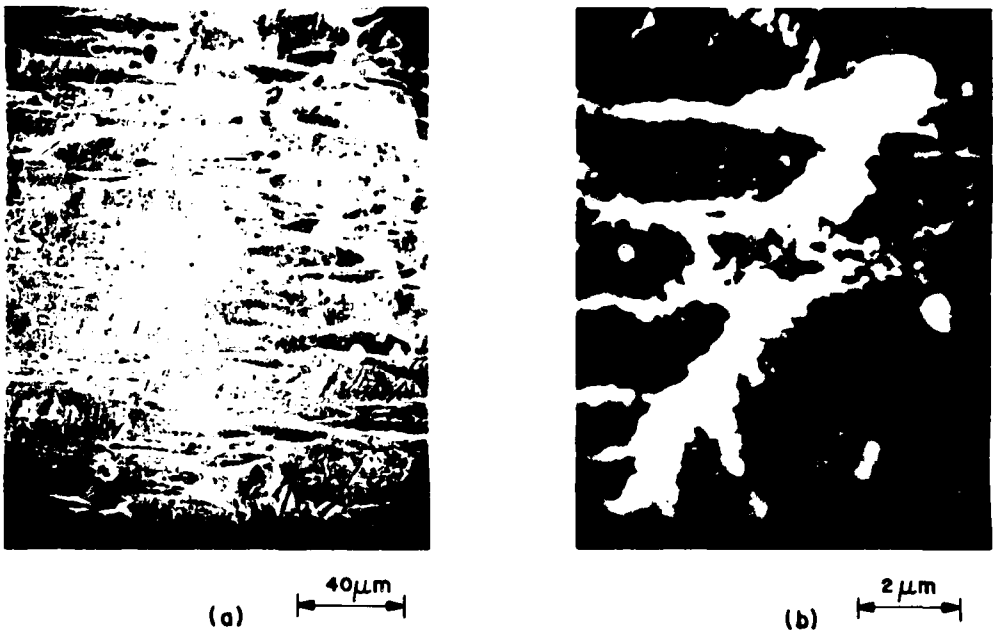

Figure 23. SEM micrographs of the shear fracture surface from an Armco iron fragment showing: (a) fracture by void growth and coalescence and (b) high-magnification view of melted asperrites.

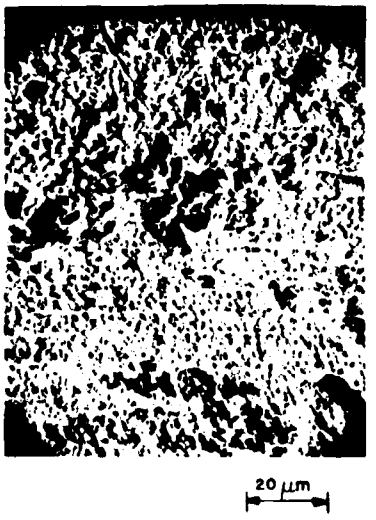

Figure 24. SEM micrograph of the shear fracture surface of an HF-1 steel fragment.

D. FRAMING CAMERA EXPERIMENT AND HEMP CODE PREDICTIONS

An attempt was made to measure the strain history of an expanding cylinder using the Moire interference technique. The 38.1-cm-long Armco iron cylinder (Table 5) was used in this test. Prior to filling the cylinder with explosive, a grid pattern and a parallel line pattern were silk screened onto the surface as shown in Figure 25. The large grid pattern consisted of 1.6-mm-wide lines over a square coordinate grid of 6.35 mm. The grid extended 6.35 cm along the cylinder axis and 17.8 cm around the circumference. The parallel line pattern consisted of a series of 0.5-mm-wide lines 12.7-cm long, oriented along the axis of the cylinder. The line spacing was 1 mm and the pattern also extended 17.8 cm around the circumference. The patterns were centered along the axis of the cylinder.

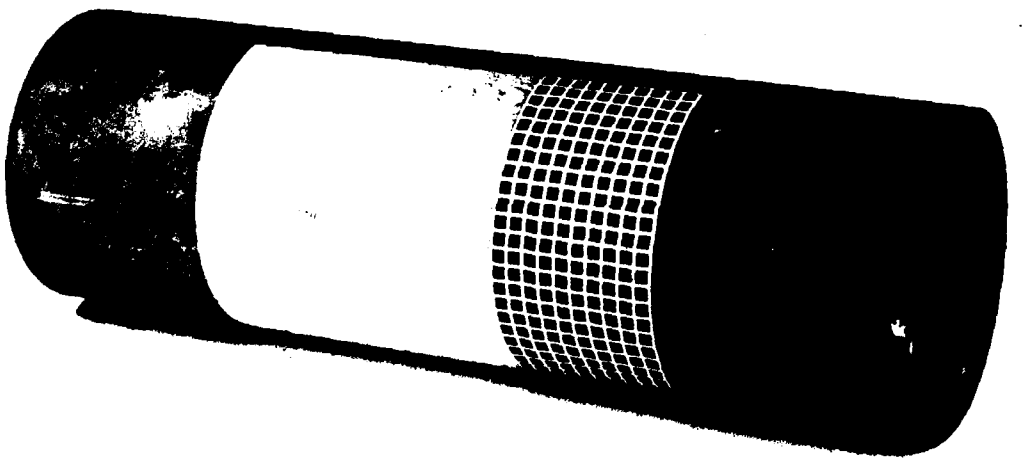

Figure 25. HF-1 steel cylinder with grids for strain measurements.

A schematic for investigating interference patterns is shown in Figure 26. A photograph of the initial pattern was used as the reference grating. This arrangement, devised by SRI, provides Moire

fringes which can be directly recorded by the framing camera when focused on the plane of the analyzing grid. It was determined, however, that this procedure could not be used because the focusing of the framing camera at the analyzer plane required the camera to be too close to the exploding cylinder.

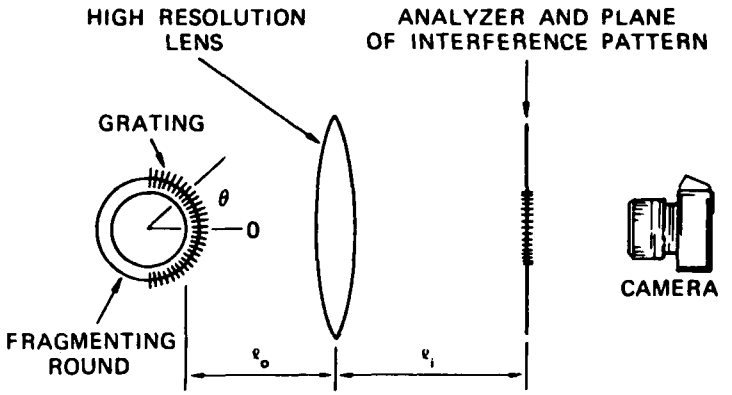

Figure 26. Schematic for optical measurement of strains (Reference 4).

The procedure that was used for the strain test was as follows: Before detonation, a series of analyzer patterns was made with the framing camera. On detonation, the event was recorded at a 4.17-μs per frame rate. The analyzer patterns were then superimposed on the detonation photographs. This procedure should have produced Moire interference fringes, but there was insufficient detail in the film to resolve the patterns. It was, nevertheless, possible to obtain the gross strain history of the cylinder by measuring its diameter on the framing camera photographs, such as Figure 27.

HEMP code calculations were performed for the expansion of both Armco iron and HF-1 steel cylinders. The results are given in Figures 28 and 29, respectively. Previous work by Coughlin[26] has shown that HEMP code calculations predict the expansion of a cylinder under explosive loading to within about 10 percent. To minimize computational difficulties,

Figure 27. Framing camera photograph of Armco iron cylinder, 56 μs after detonation.

the point of initiation was placed at the end of the metal cylinder. Strain effects on the yield stress for Armco iron were approximated by assuming the yield stress increased from 180 to 350 MPa. This assumption is quite reasonable as shown by the data of Hocket and Zukas.[34] Figure 30 is a comparison of the HEMP code calculations with results of the framing camera experiment for Armco iron.

VI. SHEAR BAND MODELS AND FRAGMENT MASS DISTRIBUTION COMPARISONS

A. INTRODUCTION

In this chapter, two models that have been developed for shear band formation in cylinder fragmentation are discussed. They are based in part on the metallographic observations that were presented in the preceding chapter. In addition, comparisons are presented for measured and computed fragment mass distributions for explosive-filled

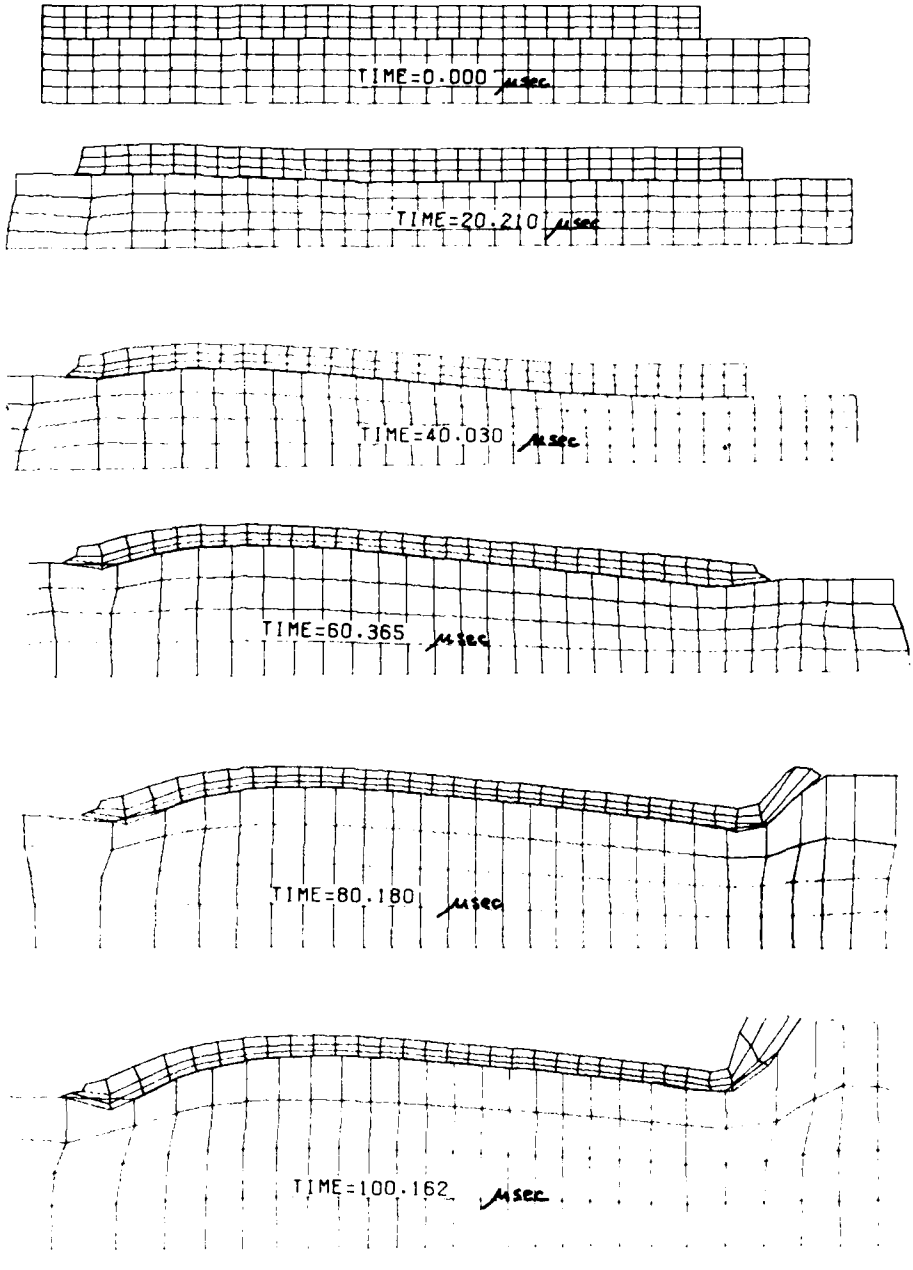

Figure 28. HEMP code predictions for Armco iron cylinders.

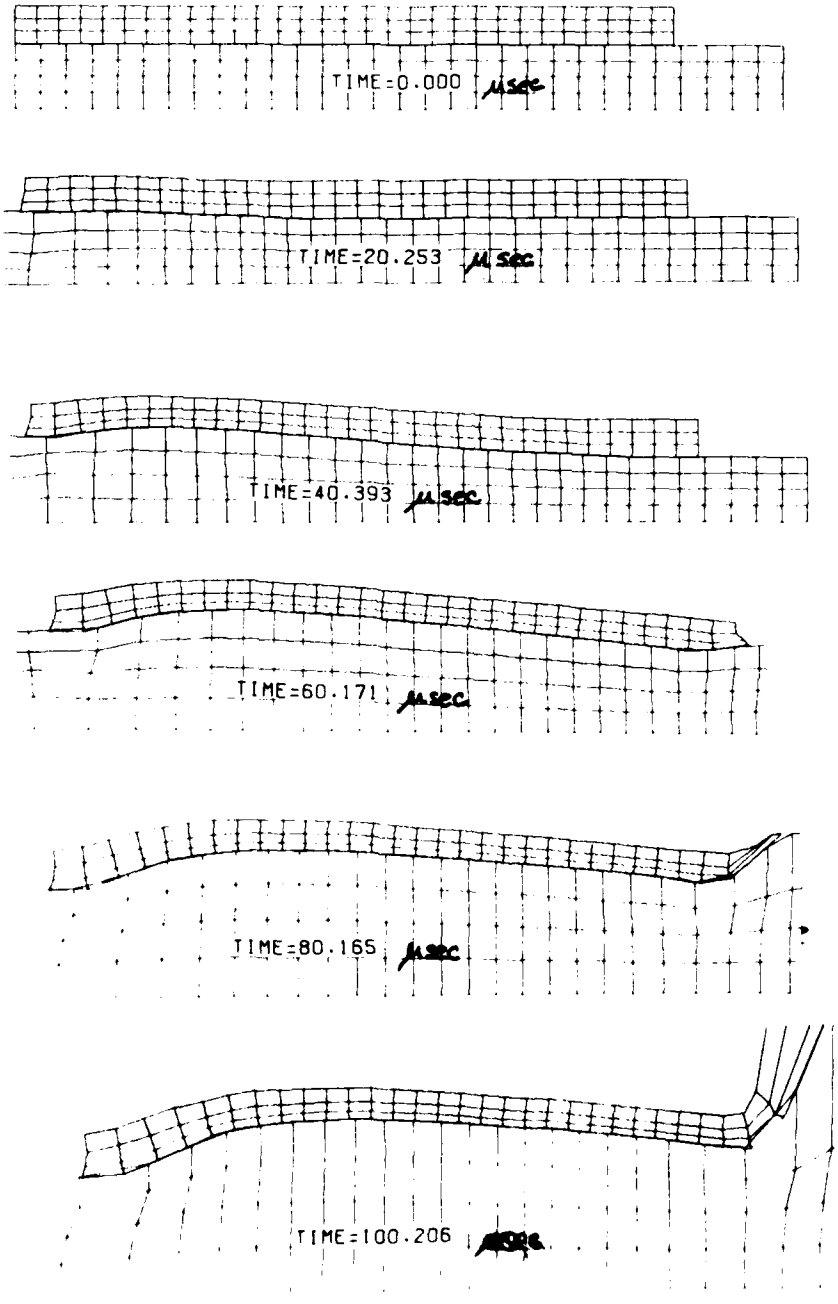

Figure 29. HEMP code predictions for HF-1 steel cylinders.

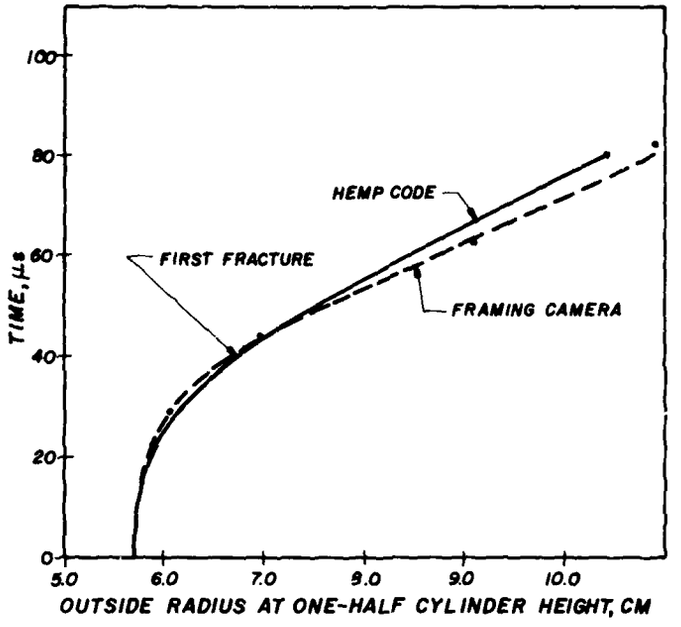

Figure 30. Comparison of framing camera results and HEMP code predictions for Armco iron cylinders.

cylinders of Armco iron and HF-1 steel. The computed mass distributions were obtained by SRI using their recently developed model for cylinder fragmentation.[4]

B. SHEAR BAND MODELS

Highly localized shear deformation has frequently been observed in metals deformed at high strain rates[33] or at cryogenic temperatures.[34,35] This type of deformation is often referred to as adiabatic shear. Zener and Holloman[33] explain the phenomena as an instability induced by the heat generated during plastic flow. The heat produces sufficient thermal softening to offset the effects of strain and strain-rate hardening and causes the deformation to concentrate in narrow bands. There are several analytical treatments of the problem in the literature;[35-40] however, none of them contain the required kinetic information necessary for calculating the propagation of shear instabilities.

A dislocation theory of unstable shear deformation has been formulated by Arsenault and Crowe.[41] This theory is based on the observation that plastic deformation in many metals and alloys is thermally activated. Consider a small cylindrical mass of material with a dislocation source on a slip plane P as shown schematically in Figure 31, the shear strain rate $\dot{\gamma}$ is given by the Orowan equation

$$\dot{\gamma} = \alpha\rho b\bar{v} \tag{7}$$

where α is the geometric factor taken as 1/2, b is the magnitude of the Burgers vector, ρ is the density of mobile dislocations on the slip plane, and $\bar{v}$ is the average dislocation velocity. ρ can be written as the mobile-line length per unit volume according to

$$\rho = \frac{N(\gamma)\pi r}{V_o} \tag{8}$$

where $N(\gamma)$ is the number of dislocations (a function of strain), r is the dislocation loop radius, and V_o is the unit volume. If the deformation proceeds by nucleation and expansion of dislocation loops from small nucleate radii to larger values r, then $r = \bar{v}t$, where t is the time of the loop expansion. Then,

$$\dot{\gamma} = \frac{b\bar{v}^2 N(\gamma)t}{V_o} \; . \tag{9}$$

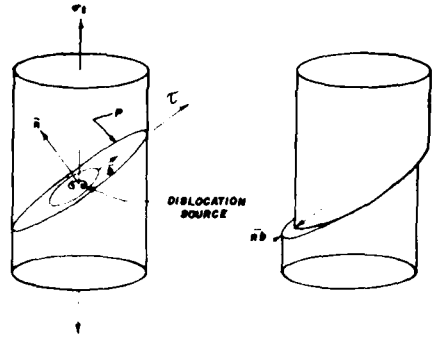

Figure 31. Schematic of shear deformation via dislocation motion on a slip plane.

According to the theory of thermally-activated plastic deformation,[42] the dislocation velocity is given by an Arrhenius equation of the form

$$\bar{v} = v_o \exp\left(\frac{-\Delta H(T,\sigma)}{kT}\right) \tag{10}$$

where ΔH is the activation enthalpy which is a function of the stress s and the absolute temperature T, k is the Boltzmann constant, and v_o is the maximum dislocation velocity.

Considering dislocation motion as a power dissipation process, the power dissipated in a small annular region about the dislocation line is

$$P = \sigma\dot{\gamma}V \tag{11}$$

where V is the volume of the annular region given approximately by $2\pi r\delta b$, where δb is the cross-sectional area of the annulus. The temperature distribution resulting from the radiating line source[43] is given as a function of position (x,y) by:

$$T(x,y) = \frac{P}{2\pi h} K_o\left(\frac{r}{\lambda}\right) \exp\left(\frac{x}{\lambda}\right) \tag{12}$$

where $K_o(r/\lambda)$ is a modified Bessel function, $\lambda = 2H/V$ is a characteristic distance, $H = \kappa/C_v$ is the thermal diffusivity, κ is the thermal conductivity, and C_v is the specific heat at constant volume. Since the dislocation velocity increases with increasing temperature, the passage of the first dislocation heats the material on the slip plane. The second dislocation emitted from the source thus travels at a slightly higher velocity than the first dislocation. If the strain rate is sufficiently high, this effect can cascade into unstable shear deformation upon subsequent dislocation emission from the source.

The above equations were programmed for an iterative solution using a finite-difference technique to solve the heat flow equations. The calculations were not completed, however, because the computer time required for a solution was prohibitively long. In principle, the above concepts provide a physically realistic description of the onset and propagation of unstable thermoplastic shear deformation. Campbell et al.[44] have shown that dislocation sources begin to operate in about 5 ns. Source operation is, therefore, probably not the rate-controlling factor, provided the dislocations leaving the source do not apply sufficient back stress to turn off source operation. For pressure durations associated with explosive loading, this is not expected to occur.

The above model is also consistent with the metallographic observations described earlier in this report. In particular, the model provides a mechanism for the nucleation of shear zones within the bulk material, since shear nuclei will occur in grains having slip systems favorably oriented with the maximum shear trajectories. The difference between the SRI and NSWC/DL observations regarding offset at the inner surface are not significant since they may only reflect the proximity of favorably oriented grains to this surface.

An important question that arises concerns the initiation of an instability at any particular location. One explanation is that each zone is associated with a local inhomogeniety which intensifies the stress on that trajectory. Another explanation is that those trajectories containing the largest number of grains favorably oriented for slip are naturally weaker, and become preferred sites of unstable shear.

The SRI approach[4, 45] to the localized shearing problem combines the bulk thermodynamic approach and the dislocation approach. This model uses a geometrically-scaled analogue of the dislocation. Figure 32 is a schematic of the model. W is the width of the shear band and B is the offset associated with shear band propagation. The kinetics of propagation are again described by the Orowan equation

$$\dot{\gamma} = N_{sb} B v_{sb} \tag{13}$$

where $\dot{\gamma}$ is the shear strain rate, N_{sb} is the density of mobile shear bands and v_{sb} is the average shear band velocity. In this formalism the governing equations [45] are

$$N_{sb} = \left[\frac{\Delta E_p/\Delta t}{E_{cr}}\right]^{3/2} \left[\frac{\rho C_v}{\kappa v_{sb}}\right] , \tag{14}$$

$$W = \left[\frac{\kappa E_{cr}}{\rho C_v \Delta E_p/\Delta t}\right]^{1/2} , \tag{15}$$

and

$$B = \left[\frac{\rho E_{cr}}{Y}\right]^{3/2} \left[\frac{\kappa}{\rho C_v \lambda}\right]^{1/2} \tag{16}$$

where ρ is the density, C_v is the specific heat at constant volume, κ is the thermal conductivity, Y is the yield stress, $\Delta E_p = C_v \Delta T$ is the plastic work, and E_{cr} is the internal energy required to remove most of the material strength.

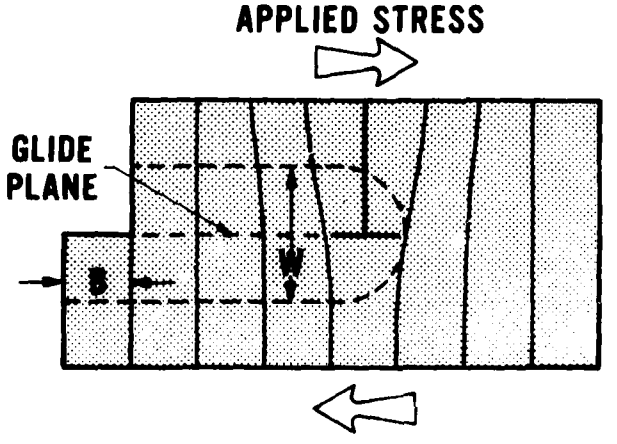

Figure 32. Schematic of shear instability as an analog of dislocation motion (Reference 45).

Values of W and B determined metallographically from recovered fragments are given in the previous chapter. These quantities should be obtainable by performing small-scale shearing experiments such as those described by Culver[46] [i.e., calculable from mechanical property and thermodynamic data and Equations (14), (15) and (16)]. At present, very little work of this type has been performed.

Another important feature of these models is that the shearing phenomena is primarily associated with a plastic deformation process and not a fracture process. In principle, the shear mechanism can operate to form new surfaces in perfect Mode II fracture propagation (the shear component of stress is applied normal to the leading edge of the crack).[47] The SEM micrographs of Figure 23 and 24 indicate that this phenomena does not occur in Armco iron and HF-1 steel. In these materials, the separation associated with the shearing phenomena probably occurs during the later stages of the fragmentation process as the tangential stress becomes tensile in the inner half-thickness regions.

C. COMPARISON OF COMPUTED AND MEASURED FRAGMENT MASS DISTRIBUTIONS

In this section, the SRI fragmentation model computations are compared with the NSWC/DL sawdust pit experiments. The procedure used to compute a fragment mass distribution for an exploding cylinder is as follows:[4]

(1) Use PUFF to calculate the elastic-plastic stress state in each undamaged element of mass.

(2) At each time step, compare computations with criteria for brittle fracture and shear band formation.

(3) If the shear band criteria are met first in an undamaged mass element, use the shear band model for subsequent computations.

(4) If the brittle fracture criteria are met first in an undamaged mass element, use the brittle fracture model for subsequent computations.

(5) Construct the fragment mass distribution by adding the crack distributions for all cells and weighting the sum by the cell mass.

The comparison of the measured and calculated fragment mass distributions for Armco iron and HF-1 steel are presented in Figures 33 and 34, respectively. As can be seen from the figures, the brittle fracture and shear band models have provided reasonable predictions of the fragment mass distributions for these materials.

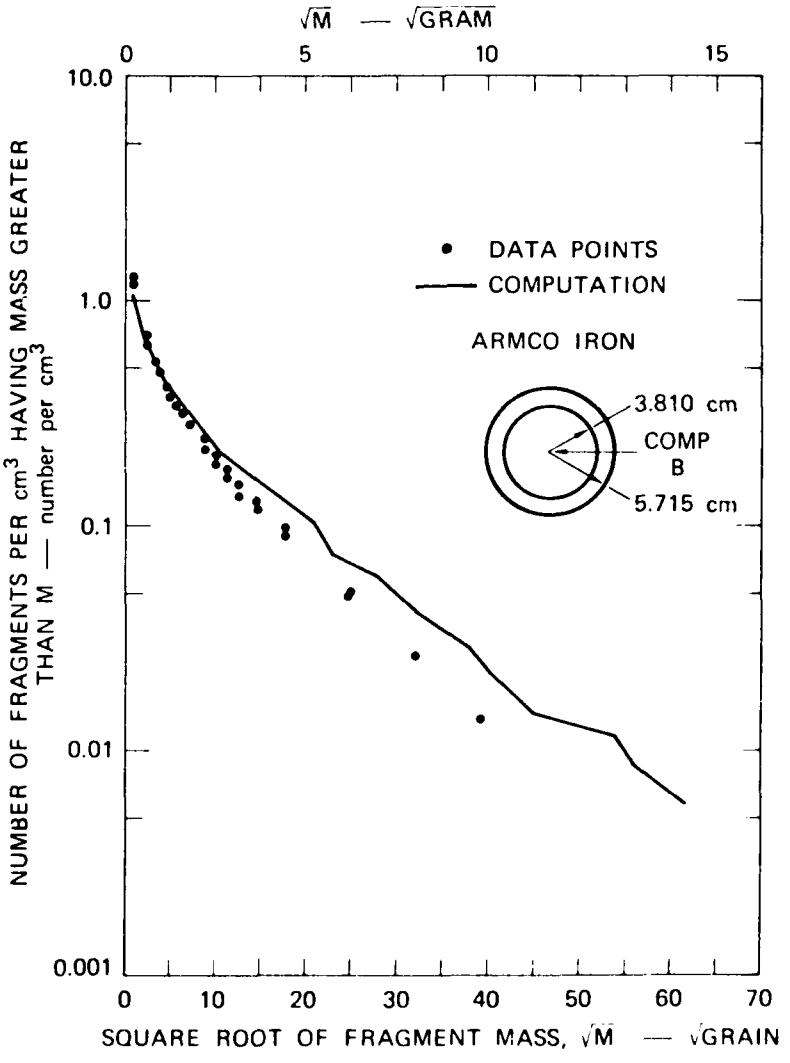

Figure 33. Comparison of measured and SRI-calculated fragment mass distributions for Armco iron (Reference 4).

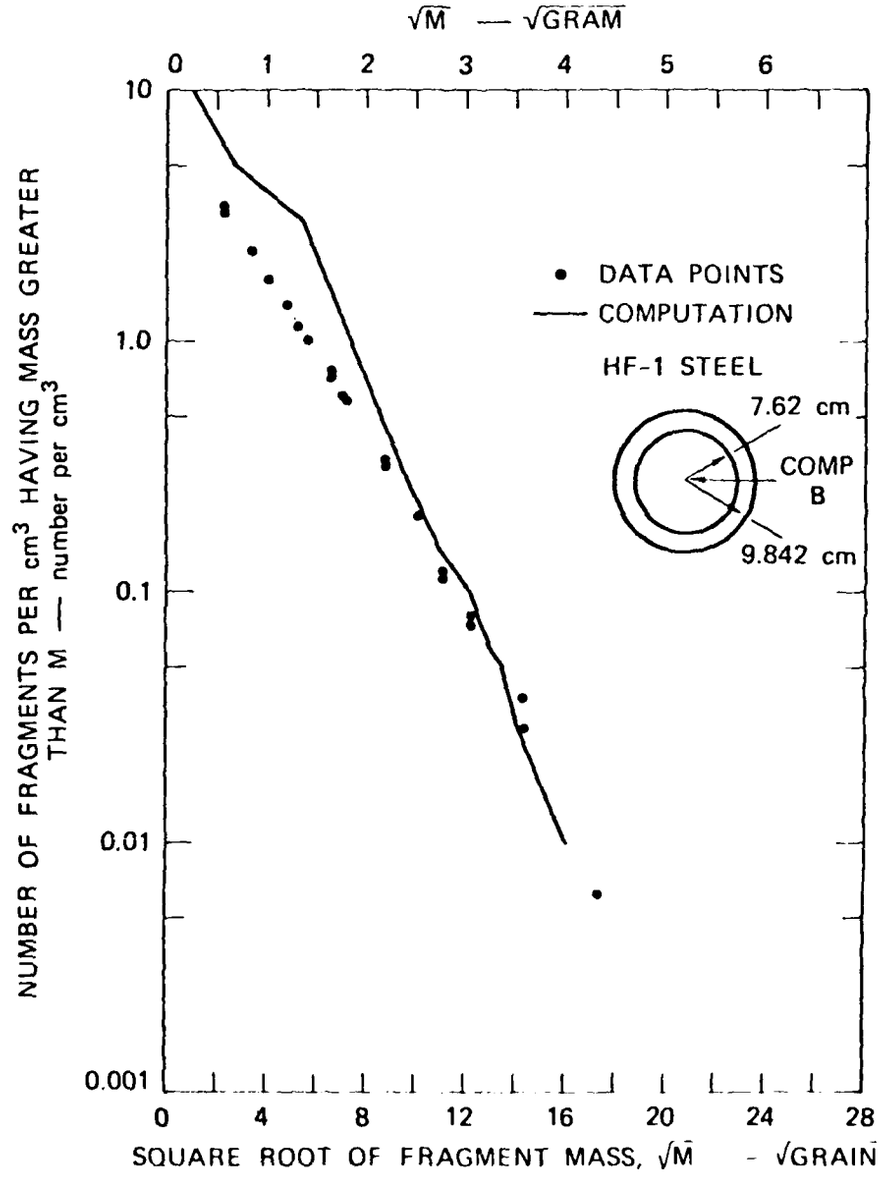

Figure 34. Comparison of measured and SRI-calculated fragment mass distributions for HF-1 steel (Reference 4).

VII. SUMMARY AND RECOMMENDATIONS

The results of this joint NSWC/DL - SRI experimental and analytical program demonstrate that the SRI fragmentation models can be used to calculate fragment mass distributions that agree favorably with experiment. These results verify the capability of newly formulated fracture and shear band models to describe fragmentation behavior. Material parameters needed in the models are obtained from dynamic experiments and thermodynamic data.

Further model refinement is needed to better match the experimental results. Additional experimental work needed includes measurement of the NAG parameters for other heat treatments to determine the sensitivity of the fragmentation model to changes in material microstructure and comparison of the calculated fragment mass distributions for these heat treatments with sawdust pit data.

REFERENCES

1. L. Seaman and D. A. Shockey, "Models for Ductile and Brittle Fracture for Two-Dimensional Propagation Calculations," AMMRC-CTR 75-2 Army Materials and Mechanics Research Center, Watertown, Massachusetts (February 1975).

2. T. W. Barbee, L. Seaman, R. Crewdson, and D. Curran, "Dynamic Fracture Criteria for Ductile and Brittle Materials," Journal of Materials, Vol. 7, p. 333 (1972).

3. D. A. Shockey, D. R. Curran, L. Seaman, J. T. Rosenberg, and C. F. Petersen, "Fragmentation of Rock Under Dynamic Loads," International Journal of Rock Mechanics and Mining Sciences and Geomechanical Abstracts, Vol. 11, p. 303 (1974).

4. L. Seaman, D. A. Shockey, D. R. Curran, and R. F. Tokheim, "Development of a Shear Band Model for Fragmentation in Exploding Cylinders," Contract N00178-74-C-0450, Naval Surface Weapons Center, Dahlgren Laboratory, Dahlgren, Virginia (August 1975).

5. G. I. Taylor, "Analysis of the Explosion of a Long Cylindrical Bomb Detonated at One End," The Scientific Papers of G. I. Taylor, Vol. 3, edited by G. K. Batchelor, Cambridge University Press (1963) p. 277.

6. G. I. Taylor, "The Fragmentation of Tubular Bombs," The Scientific Papers of G. I. Taylor, Vol. 3, edited by G. K. Batchelor, Cambridge University Press (1963) p. 387.

7. N. F. Mott and E. H. Linfoot, "A Theory of Fragmentation," AC 3348 Ministry of Supply, London, Great Britain (1943).

8. N. F. Mott, "A Theory of the Fragmentation of Shells and Bombs," AC 4035, Ministry of Supply, London, Great Britain (1944).

9. N. F. Mott, "Fragmentation of Shell Cases," Proceedings of the Royal Society, Vol. 189A, p. 300 (1947).

10. A. A. Griffith, "The Phenomena of Rupture and Flow in Solids," Philosophical Transactions of the Royal Society, Vol. 221, p. 163 (1921).

11. J. S. Rinehart and J. Pearson, The Behavior of Metals Under Impulsive Loads, American Society for Metals, Metals Park, Ohio (1954).

REFERENCES (Continued)

12. C. R. Hoggatt and R. F. Recht, "Fracture Behavior of Tubular Bombs," Journal of Applied Physics, Vol. 39, p. 1856 (1968).

13. E. E. Banks, "Fragmentation Behavior of Thin-Walled Metal Cylinders," Journal of Applied Physics, Vol. 40, p. 437 (1969).

14. J. S. Rinehart and J. Pearson, Explosive Working of Metals, MacMillan Company, New York (1963).

15. S. Kronman, "Flash X-ray Technique for Evaluating Fragmentation," Paper presented at the Fragmentation Technology Seminar, Army Materials and Mechanics Research Center, Watertown, Massachusetts (October 1968).

16. E. N. Clark, "Properties of Materials Under High Strain Rates," paper presented at the Fragmentation Technology Seminar, Army Materials and Mechanics Research Center, Watertown, Massachusetts (October 1968).

17. E. N. Clark and I. P. Juriaco, "Mechanics of Fragmentation of Cylinders," Proceedings of the Army Symposium on Solid Mechanics, MS 73-2, Army Materials and Mechanics Research Center (September 1973).

18. R. A. Meinert, "Total Extension Curves for High Fragmentation Steels," paper presented at the Metallurgical Investigation for Improved Shell Fragmentation Meeting, Picatinny Arsenal, Dover, New Jersey (November 1967).

19. B. P. Bardes, "Mechanisms of Fragmentation of Silico-Manganese Steels," R-1918, Frankford Arsenal, Philadelphia, Pennsylivania (1969).

20. S. F. Magis, "Second Partial Report: Material Selection for Naturally Fragmenting Munitions," NWL T-24/65, Naval Weapons Laboratory, Dahlgren, Virginia (1965).

21. S. F. Magis, "Material Selection for Naturally Fragmenting Munitions," NWL T-13/67, Naval Weapons Laboratory, Dahlgren, Virginia (1967).

22. A. J. Bedford, "The Natural Fragmentation of Steel Cylinders with Tempered Martensite Microstructures," Report 532, Department of Supply, Maribyrnong, Australia (December 1972).

23. B. Walsh, "The Influence of Geometry on the Natural Fragmentation of Steel Cylinders," Report 533, Department of Supply, Maribyrnong, Australia (January 1973).

REFERENCES (Continued)

24. F. E. Allison and R. W. Watson, "Explosively Loaded Metallic Cylinders I," Journal of Applied Physics, Vol. 34, p. 842 (1960).

25. R. P. O'Shea, "Development of Naturally Fragmenting Materials," paper presented at the Fragmentation Technology Seminar, Army Materials and Mechanics Research Center, Watertown, Massachusetts (October 1968).

26. J. R. Coughlin, private communication, Naval Surface Weapons Center, Dahlgren Laboratory, Dahlgren, Virginia.

27. D. A. Shockey, L. Seaman, and D. R. Curran, "Dynamic Fracture of Beryllium Under Plate Impact and Correlations with Electron Beam and Underground Test Results," AFWL-TR-73-12, Air Force Weapons Laboratory, Kirtland Air Force Base, New Mexico (January 1973).

28. W. Mock, Jr. and W. H. Holt, "The NSWC Gas Gun Facility for Shock Effects in Materials," NSWC/DL TR-3473, Naval Surface Weapons Center, Dahlgren Laboratory, Dahlgren, Virginia (July 1976).

29. W. Mock, Jr., W. H. Holt, and C. R. Crowe, "Dynamic Yield Stress and Elastic Wave Velocity Measurements for HF-1 Steel," NSWC/DL TR-3519, Naval Surface Weapons Center, Dahlgren Laboratory, Dahlgren, Virginia (September 1976).

30. W. H. Holt and W. Mock, Jr., "Soft Recovery of Shocked Specimens for Dynamic Fracture Studies," Review of Scientific Instruments, Vol. 47, p. 210 (1976).

31. D. J. Ammerman, "Fragmentation Test Facilities, Methods and Data Processing Used at NWL," NWL TN-T-2/73, Naval Weapons Laboratory, Dahlgren, Virginia (1973).

32. E. P. Dahlberg, "Techniques for Cleaning Service Failures in Preparation for Scanning Electron Microscope and Microprobe Analysis," Scanning Electron Microscopy, edited by O. Johari and I. Corvin, IIT Research Institute, Chicago (1974) p. 911.

33. C. Zener and J. H. Hollomon, "Plastic Flow and Rupture of Metals," ASM Transactions, Vol. 33, p. 162 (1944).

34. J. E. Hockett and E. G. Zukas, "The Response of Iron to Dynamic Compression," Mechanical Properties at High Rates of Strain, edited by J. Harding, The Institute of Physics, London (1974) p. 53.

REFERENCES (Continued)

35. Z. S. Basinski, "The Instability of Plastic Flow of Metals at Very Low Temperatures," Proceedings of the Royal Society, Vol. 240A, p. 229 (1957).

36. R. F. Recht, "Catastrophic Thermoplastic Shear," Journal of Applied Mechanics, Vol. 31, p. 189 (1964).

37. J. Pomey, "Plasticite et Construction Mechanique," Rev. Francaise de Mechanique, No. 12, p. 5 (1964).

38. V. S. Shankhla and R. F. Scrutton, "The Free Plastic Compression of Pure Metals," Journal of Applied Mechanics, Vol. 36, p. 1121 (1970).

39. B. F. von Turkovich, "Mechanics of Cutting," Society of Mechanical Engineers, MR71-903 (1971).

40. L. P. Kubin and B. Jouffrey, "On Low Temperature Plastic Instability in Pure Niobium Single Crystals," Philosophical Magazine, Vol. 24, p. 437 (1971).

41. C. R. Crowe, "Shear Band Model for Fragmentation," paper presented at the Ballistics Research Laboratory, Aberdeen Proving Ground, Maryland (October 1974).

42. H. Conrad, "Thermally Activated Deformation of Metals," Journal of Metals, Vol. 16, p. 582 (1964).

43. J. D. Eshelby and P. L. Pratt, "Note on the Heating Effect of Moving Dislocations," Acta Metallurgica, Vol. 4, p. 560 (1956).

44. J. D. Campbell, J. A. Simmons, and J. E. Dorn, "On the Dynamic Behavior of a Frank-Read Source," Journal of Applied Mechanics, Vol. 83, p. 447 (1961).

45. D. R. Curran, D. A. Shockey, and L. Seaman, "The Windjammer or SNAG Model for Adiabatic Shear Banding," private communication, Stanford Research Institute, Menlo Park, California (November 1974).

46. R. S. Culver, "Thermal Instability Strain in Dynamic Plastic Deformation," Metallurgical Effects at High Strain Rates, edited by R. W. Rhode, B. M. Butcher, J. R. Holland, and C. H. Karnes, Plenum Press, New York (1973) p. 519.

47. A. S. Tetelman and A. J. McEvily, Jr., Fracture of Structural Materials, John Wiley and Sons, Inc., New York (1967).

DISTRIBUTION

Defense Documentation Center
Cameron Station
Alexandria, VA 21314 (12)

Defense Printing Service
Washington Navy Yard
Washington, DC 20374

Library of Congress
Washington, DC 20540
Attn: Gift and Exchange Division (4)

Commander
Naval Sea Systems Command
Washington, DC 20360
Attn: SEA-0333 (W. W. Blaine)
0333 (R. A. Bailey)
035 (G. N. Sorkin)
9921C (L. Hawver)

Commander
Naval Air Systems Command
Washington, DC 20360
Attn: AIR-310B (J. W. Willis)
320A (T. F. Kearns)
350 (E. M. Fisher)
350D (H. B. Benefiel)

Commander
Naval Weapons Center
China Lake, CA 93555
Attn: J. Pearson
M. E. Backman
S. A. Finnegan

Director
Army Ballistics Research Laboratories
Terminal Ballistics Laboratory
Aberdeen Proving Ground, MD 20015
Attn: A. Dietrich
W. Gillich
G. Moss
R. Vitali

DISTRIBUTION (Continued)

Commander
Army Materials and Mechanics Research Center
Watertown, MA 02172
Attn: J. F. Mescall
P. V. Riffin

Commander
Army Picatinny Arsenal
Dover, NJ 08901
Attn: E. N. Clark

Commanding Officer
Air Force Armament Laboratory
Eglin AFB, FL 32542
Attn: DLY
DLJ
DLJW (McKenney)

Director
Defense Advanced Research Projects Agency
1400 Wilson Blvd.
Arlington, VA 22209
Attn: E. Blaise
C. Lehner

Stanford Research Institute
Poulter Laboratory
333 Ravenswood Avenue
Menlo Park, CA 94025
Attn: D. Curran
D. Shockey
L. Seaman
R. Tokheim

Local:

CC
CD
DC
DD
DG
DG-10
DG-13
DG-20
DG-30
DG-33

DISTRIBUTION (Continued)

DG-33 (Thompson)	
DG-34	
DG-40	
DG-41	
DG-50	
DG-51	
DG-52	
DG-52 (Mock)	(2)
DG-52 (Holt)	(2)
DG-52 (Wishard)	
DG-53	
DG-53 (Wenborne)	
DG-53 (Payne)	
DG-55	
DK-70	
DK-74 (Griffin)	(2)
DN	
DN-40	
DX-21	(2)
DX-222	(6)
DX-40	
DX-43 (Hall)	
WR	
WR-10	
WR-12 (Anderson)	
WR-13	
WR-13 (Forbes)	
WR-30	
WR-32	
WR-32 (Crowe)	(2)
WR-34	